Kinetic ballooning/interchange instability in a bent plasma sheet

E. V. Panov,[1] R. Nakamura,[1] W. Baumjohann,[1] M. G. Kubyshkina,[2] A. V. Artemyev,[3] V. A. Sergeev,[2] A. A. Petrukovich,[3] V. Angelopoulos,[4] K.-H. Glassmeier,[5,6] J. P. McFadden,[7] and D. Larson[7]

Received 29 December 2011; revised 27 April 2012; accepted 1 May 2012; published 28 June 2012.

[1] We use Time History of Events and Macroscale Interactions during Substorms (THEMIS) and GOES observations to investigate the plasma sheet evolution on 28 February 2008 between 6:50 and 7:50 UT, when there developed strong magnetic field oscillations with periods of 100 s. Using multispacecraft analysis of the plasma sheet observations and an empirical plasma sheet model, we determine both the large-scale evolution of the plasma sheet and the properties of the oscillations. We found that the oscillations exhibited signatures of kinetic ballooning/interchange instability fingers that developed in a bent current sheet. The interchange oscillations had a sausage structure, propagated duskward at a velocity of about 100 km/s, and were associated with fast radial electron flows. We suggest that the observed negative gradient of the Z_{GSM} magnetic field component ($\partial B_Z/\partial X$) was a free energy source for the kinetic ballooning/interchange instability. Tens of minutes later a fast elongation of ballooning/interchange fingers was detected between 6 and 16 R_E downtail with the length-to-width ratio exceeding 20. The finger elongation ended with signatures of reconnection in an embedded current sheet near the bending point. These observations suggest a complex interplay between the midtail and near-Earth plasma sheet dynamics, involving localized fluctuations in both cross-tail and radial directions before current sheet reconnection.

Citation: Panov, E. V., et al. (2012), Kinetic ballooning/interchange instability in a bent plasma sheet, *J. Geophys. Res.*, *117*, A06228, doi:10.1029/2011JA017496.

1. Introduction

[2] Loading and unloading of Earth's magnetotail, which occur periodically, generate magnetic substorms [*Baker et al.*, 1996]. Plasma sheet loading occurs during the substorm growth phase. At this stage the plasma sheet stretches [e.g., *Mishin et al.*, 2001; *Petrukovich et al.*, 2007], perhaps due to increasing magnetic flux in the lobes or during development of magnetotail current sheet instability. When the stresses collected during plasma sheet loading are too large, plasma sheet unloading occurs during the substorm expansion phase through magnetotail reconnection.

[3] Reconnection can occur at near-Earth radial distances (up to about 30 R_E downtail) [see, e.g., *Nagai et al.*, 2005] and also in the distant tail. One of the best observations of reconnection was made recently by THEMIS (Time History of Events and Macroscale Interactions during Substorms) probes (P1–P5) [*Angelopoulos et al.*, 2008]. A conventional reconnection scenario, development of a tearing instability in a one-dimensional ($\partial B_Z/\partial X \approx 0$) current sheet [*Coppi et al.*, 1966; *Schindler*, 1974; *Zelenyi et al.*, 2008, and references therein], appears to agree with Cluster observations of thin current sheets at around 19 R_E downtail [*Zelenyi et al.*, 2010].

[4] Bursty bulk flows (BBFs), fast plasma flows inside the plasma sheet generated by reconnection [*Hayakawa et al.*, 1982; *Baumjohann et al.*, 1989, 1990; *Angelopoulos et al.*, 1992, 1994], can transport Earthward flux efficiently and are associated with substorms [*Baumjohann et al.*, 1991, 1999]. Multispacecraft observations have revealed that BBFs occur in very localized channels up to 2–3 R_E wide [*Angelopoulos et al.*, 1996; *Sergeev et al.*, 1996; *Nakamura et al.*, 2004; *Snekvik et al.*, 2007]. Vortices are created on both sides of these channels [*Keika et al.*, 2009; *Keiling et al.*, 2009; *Panov et al.*, 2010a, 2010b; *Birn et al.*, 2011].

[5] At around 10 R_E, BBFs are suddenly decelerated by the dominant dipolar magnetic field, and pressure gradients pile up, leading to a substorm current wedge [see, e.g.,

[1]Space Research Institute, Austrian Academy of Sciences, Graz, Austria.
[2]St. Petersburg State University, St. Petersburg, Russia.
[3]Space Research Institute of Russian Academy of Sciences, Moscow, Russia.
[4]Institute of Geophysics and Planetary Physics, University of California, Los Angeles, California, USA.
[5]Institut für Geophysik und Extraterrestrische Physik, Technische Universität Braunschweig, Braunschweig, Germany.
[6]Max-Planck-Institute for Solar System Research, Katlenburg-Lindau, Germany.
[7]Space Science Laboratory, University of California, Berkeley, California, USA.

Corresponding author: E. V. Panov, Space Research Institute, Austrian Academy of Sciences, Schmiedlstr. 6, AT-8042 Graz, Austria. (evgeny.panov@oeaw.ac.at)

0148-0227/12/2011JA017496

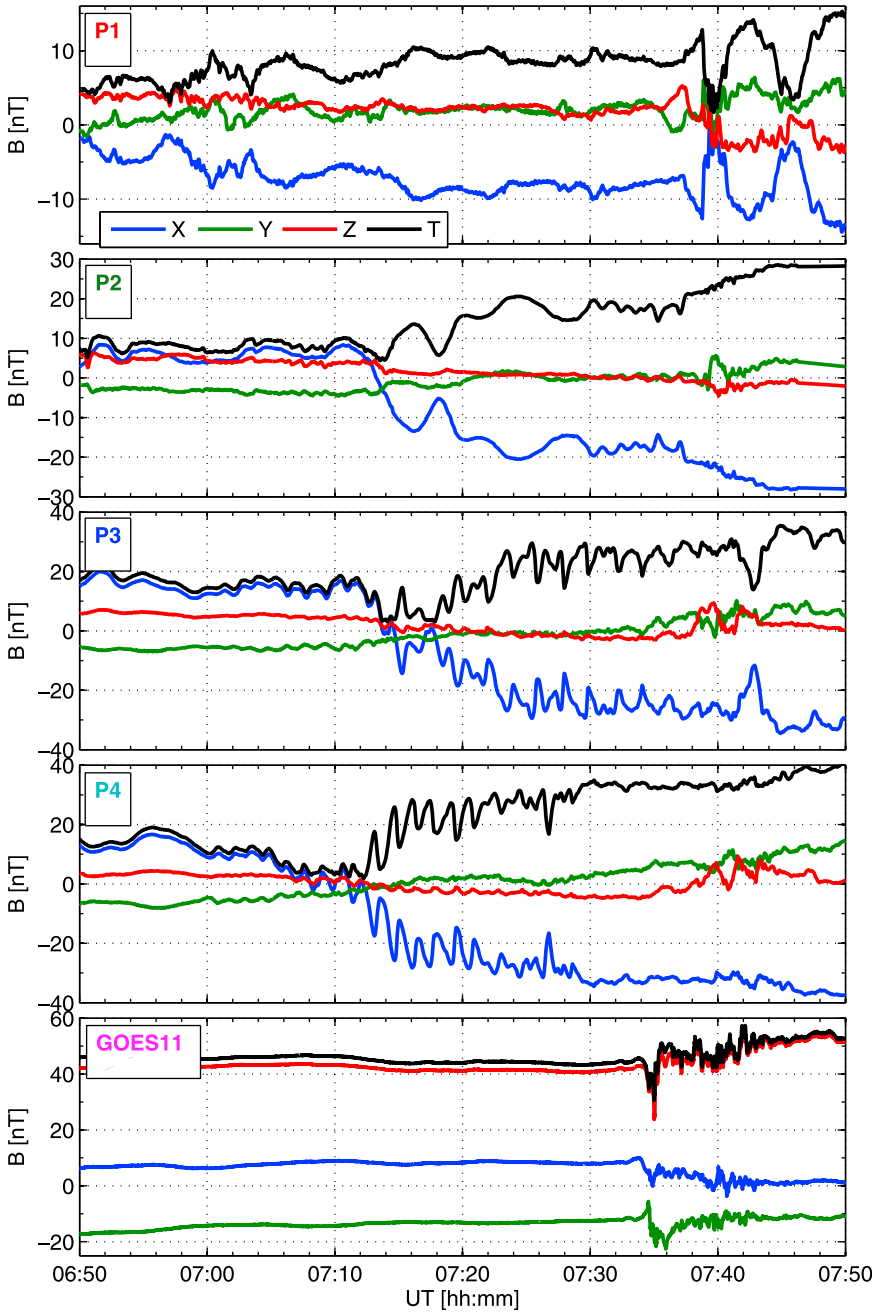

Figure 1. GSM components of the magnetic field from P1–P4 THEMIS and GOES 11 spacecraft on 28 February 2008 between 6:50 and 7:50 UT. See legend for color coding.

Baumjohann, 2002] and substorm onset. As BBFs decelerate, they can oscillate [*Chen and Wolf*, 1999; *Panov et al.*, 2010b; *Birn et al.*, 2011]. When they arrive at the inner edge of the plasma sheet, the magnetotail dipolarizes [*Nakamura et al.*, 1994; *Schödel et al.*, 2001a, 2001b; *Baumjohann*, 2002; *Nakamura et al.*, 2002, 2004; *Kaufmann et al.*, 2005; *Ohtani et al.*, 2006; *Takada et al.*, 2006; *Kaufmann and Paterson*, 2008]. Dipolarization is first observed in the near-Earth plasma sheet and then moves tailward [*Baumjohann et al.*, 1999; *Birn et al.*, 2011].

[6] Detailed studies of reconnection closer to Earth have been done. While studying several reconnection events using Cluster and Double Star data, *Sergeev et al.* [2008] found that the plasma sheet may reconnect as close as 12 R_E downtail. *Petrukovich et al.* [2009] showed that if observations are limited to a thin current sheet, reconnection starts primarily inside 20 R_E. For reconnection at such small distances, *Lui et al.* [1992] and *Lui* [1996] proposed a 'current disruption model' that suggests that reconnection will be triggered by an instability. There is, however, no final agreement on the

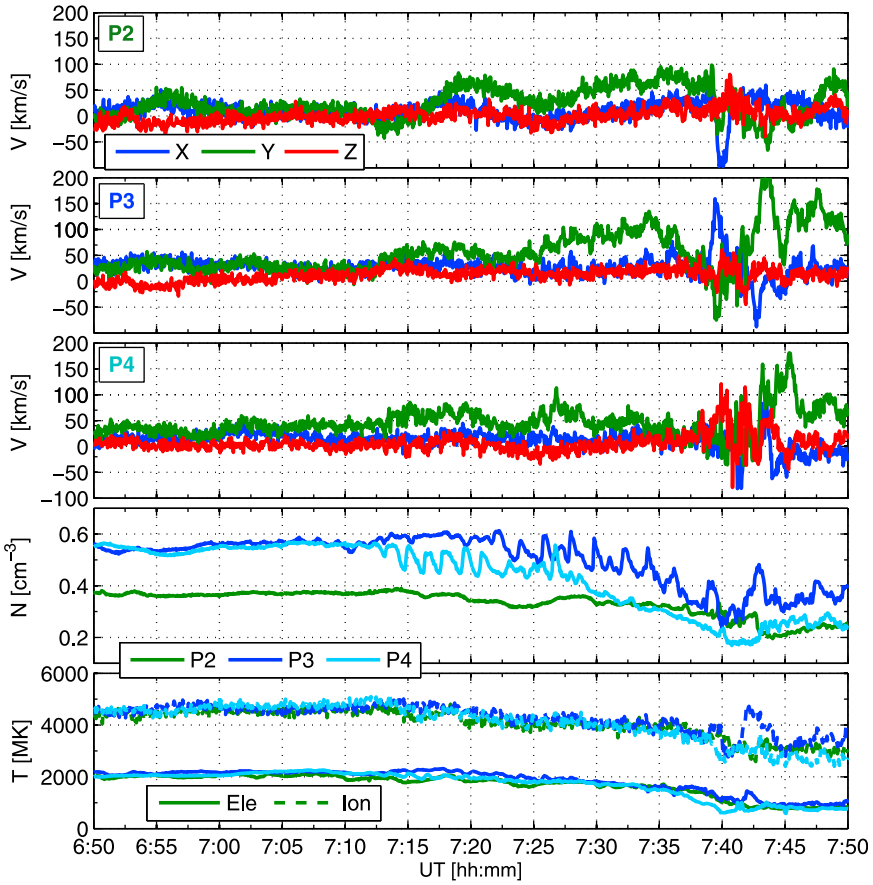

Figure 2. GSM components of the ion velocity, the electron density, and the ion and electron temperatures (joint ESA and SST moments) from three THEMIS probes (on board P1 ESA and SST spectrometer data were not downlinked for this time; P5 was deep in the inner magnetosphere) on 28 February 2008 between 6:50 and 7:50 UT. See legends for color coding.

nature of the instabilities operating in this region of the magnetotail [e.g., *Baumjohann et al.*, 2007].

[7] It has been suggested that a ballooning/interchange process could play a crucial role in development of current-disrupting instability [*Roux et al.*, 1991; *Cheng and Lui*, 1998; *Liang et al.*, 2008; *Saito et al.*, 2008]. Kinetic simulations have shown that negative values of $\partial B_Z/\partial X$ can be a free energy source for kinetic ballooning/interchange instability [*Pritchett and Coroniti*, 2010].

[8] *Hurricane et al.* [1999] predicted that ballooning/interchange instabilities could be linearly unstable when the interchange mechanism takes place in a very elongated space. For such a case they found that the instability would grow infinitely in a short time, perhaps 'detonating' a substorm. *Pritchett and Coroniti* [2011] demonstrated that a kinetic ballooning/interchange instability can lead to near-Earth reconnection in the plasma sheet. And, indeed, *Yang et al.* [2011] and *Hu et al.* [2011] found that an interchange mechanism would accelerate plasma sheet thinning, which may facilitate reconnection.

[9] In this paper we employ the observations of five identical THEMIS [*Angelopoulos*, 2008] probes from 28 February 2008 between 6:50 and 7:50 UT to study *in situ* kinetic ballooning/interchange instability that grew in a bent plasma sheet with negative $\partial B_Z/\partial X$. We also discuss a possible reconnection scenario that was observed during instability development between 11 and 16 R_E downtail and is associated with a substorm onset.

2. Plasma Sheet Evolution Leading to Substorm Onset

[10] For our analysis we used 3 s spin resolution data. The magnetic field measurements were collected by THEMIS fluxgate magnetometers (FGM) [*Auster et al.*, 2008]. The ion and electron distribution functions were sampled by THEMIS Electrostatic Analyzers (ESA) [*McFadden et al.*, 2008] for particles with energies less than 30 keV and by THEMIS Solid State Telescopes (SST) for particles with energies more than 30 keV. We used the combined ESA and SST ion moments to improve the quality of the ion and electron moment data. The X and Y components of the electric field from the Electric Field Instrument (EFI) [*Bonnell et al.*, 2008] were also used.

[11] Figures 1 and 2 present magnetic field and particle measurements by THEMIS and GOES 11 on 28 February 2008 between 6:50 and 7:50 UT. During this interval the spacecraft were located as follows: R_{P1} = (−25.2; 16.0; −5.2) R_E, R_{P2} = (−15.8; 3.0; −3.1) R_E, R_{P3} = (−11.2; 2.1; −2.5) R_E, R_{P4} = (−11.1; 3.1; −2.5) R_E, R_{P5} = (−4.9; −2.3; −1.4) R_E, R_{GOES11} = (−6.1; 3.0; −1.1) R_E. We further use GOES 11

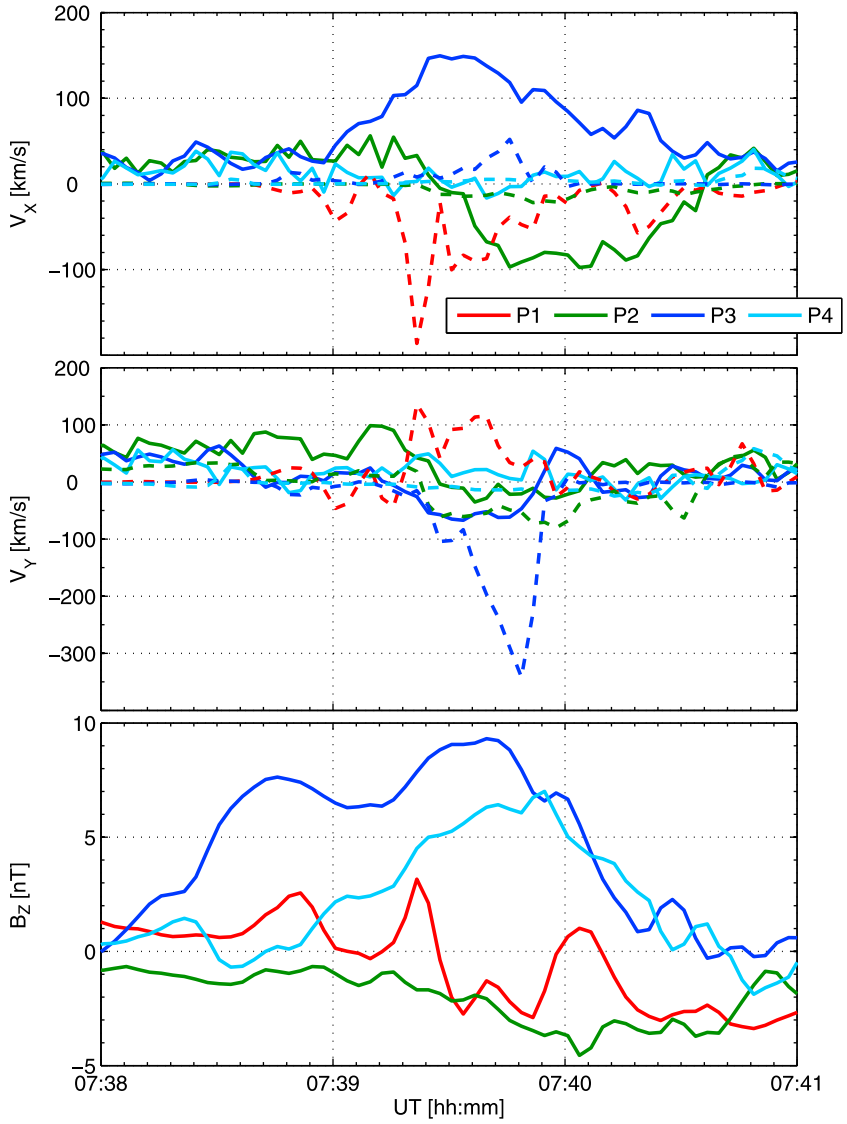

Figure 3. (top) X_{GSM} and (middle) Y_{GSM} components of the plasma velocity (solid lines) and the **E** × **B**-drift velocity (dashed lines). (bottom) Z_{GSM} component of the magnetic field from THEMIS P1, P2, P3, and P4 on 28 February 2008 between 7:38 and 7:41 UT.

data instead of P5 because it was located at a closer MLT to the other THEMIS probes.

[12] Figure 1 shows the X_{GSM}, Y_{GSM}, and Z_{GSM} components of the magnetic field vector and the total magnetic field (see legend for color coding). The panels are ordered from greater to smaller distances of the spacecraft from the Earth; i.e, from about 29 to 6 R_E downtail. One can see from the figure that at about 7:15 UT, P1, P2, P3, and P4 moved southward with respect to the neutral sheet, while GOES 11 was located in the inner magnetosphere. Also, starting at about 7:00 UT, P3 and P4 clearly observed oscillations with periods of about 100 s in the X_{GSM} component of the magnetic field. At around 7:30 UT, P2 and GOES 11 began to observe similar oscillations. Finally, at about 7:40 UT, strong disturbances in all magnetic field components were observed simultaneously by P1, P2, P3, and P4.

[13] Three GSM components of the ion bulk velocity from P2, P3, and P4 are shown in the first three panels of Figure 2. Onboard P1, ESA and SST spectrometer data were not downlinked for this time. Note that after 7:10 UT the probes located in the plasma sheet (P2, P3, and P4), detected growth of the Y_{GSM} ion velocity component, which may indicate cross-tail current growth. At around 7:40 UT the three probes observed stronger flows with speeds exceeding 200 km/s mainly along the X_{GSM} and Y_{GSM} axes. P5 observed mainly noise-like velocity oscillations of inner magnetosphere plasma. For completeness of the particle observations we also show electron density and ion and electron temperatures in the fourth and fifth panels of Figure 2.

[14] The top and middle panels in Figure 3 show the X_{GSM}- and Y_{GSM}-plasma velocity components (solid lines) and the **E** × **B**-drift velocity (dashed lines) observed by P1, P2, P3, and P4 on 28 February 2008 between 7:38 and 7:41 UT. To fill the gap in the P1 plasma observations, we used electric field measurements from the EFI instrument to obtain the **E** × **B**-drift velocity. The EFI instrument

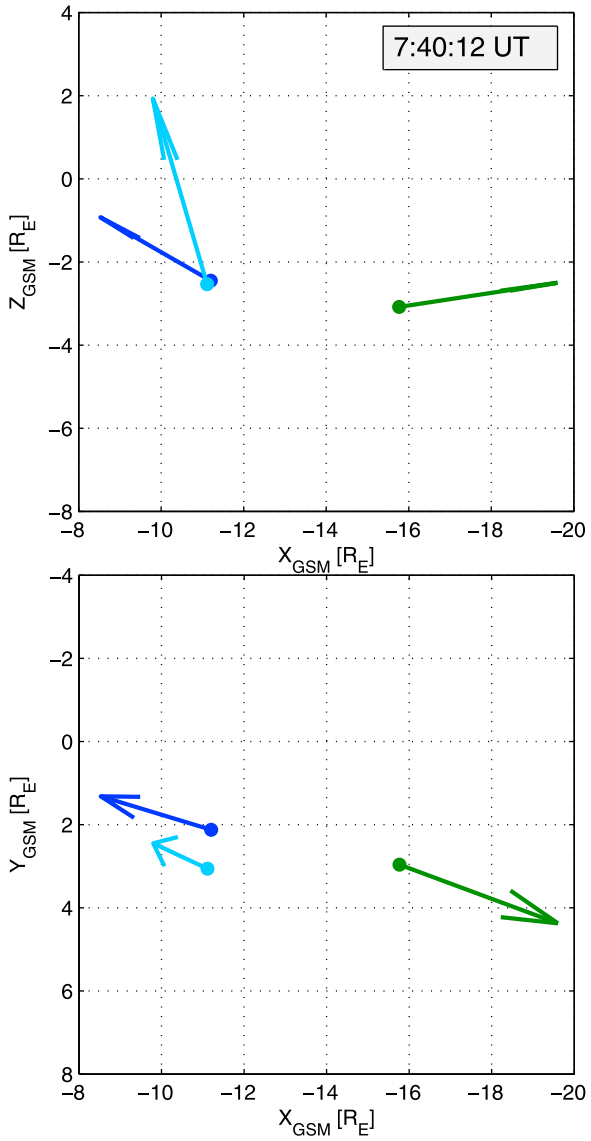

Figure 4. Velocity flows at THEMIS P2 (green lines), P3 (blue lines), and P4 (cyan lines) on 28 February 2008 at 7:40:12 UT.

originally measures only two components of the electric field vector in the plane perpendicular to the probe spin axis. We calculated the third component of the electric field assuming that $E \cdot B = 0$.

[15] Whereas the probe located closer to Earth (P3) observed Earthward flows, the tailward probes (P1 and P2) observed tailward flows. This observation suggests that the plasma sheet reconnected between 11 and 16 R_E downtail.

[16] The bottom panel of Figure 3 shows the Z_{GSM} component of the magnetic field. Observations of that component support the idea about reconnection: while the more Earthward probes (P3 and P4) observed positive enhancements in the B_Z up to 10 nT, the more tailward probes (P1 and P2) observed negative B_Z down to −5 nT.

[17] Figure 4 shows the velocity flows at P2 (green), P3 (blue), and P4 (cyan) at 7:40:12 UT. Those at P2 and P3 were observed simultaneously and always on nearly the same line, but were directed oppositely. Therefore the flow at P2 cannot be explained as a reflection beam. In addition, velocity vectors pattern in the $(X, Y)_{GSM}$ plane also does not show vortical signatures.

[18] Simultaneously with the flows, the THEMIS ground-based magnetometer network observed a formed current wedge (shown in section 3.4) at the foot points of the field lines leading to the THEMIS probes.

2.1. Plasma Sheet Bending, Embedding, and Dipolarization

[19] In the previous section we noted that after 7:10 UT P1, P2, P3, and P4 moved more southward with respect to the neutral sheet plane. To understand the major plasma sheet dynamics that caused this movement, we employed the adapted Tsyganenko model [*Kubyshkina et al.*, 2009]; more exactly, the AM-03 version of the model, in which we used the total pressure measurements by P2 (i.e., at about 16 R_E downtail) as an estimate for the lobe magnetic field. Estimating the lobe magnetic field allows reconstruction of a thin current sheet [see *Kubyshkina et al.*, 2011, for details]. Magnetic field measurements from THEMIS probes were taken as input spacecraft data also.

[20] Figure 5 shows the magnetic field lines predicted by the AM-03 model in the noon meridian $(X, Z)_{GSM}$ plane on 28 February 2008 at 7:01 UT, 7:20 UT, 7:23 UT, 7:38 UT, and 7:39 UT. The locations of the four THEMIS probes and GOES 11 spacecraft are overplotted (see legend for color coding). One can see that at 7:01 UT the plasma sheet neutral plane was approximately perpendicular to the Earth's magnetic dipole at all X_{GSM} coordinates covered by THEMIS probes; i.e., from −25 to −5 R_E.

[21] At about 7:12 UT the part of the plasma sheet at $X <$ −10 R_E started to move northward. The final stage of this movement is shown in the second panel in Figure 5, which demonstrates the plasma sheet geometry at 7:20 UT. Because the magnetic dipole was tilted tailward in the northern hemisphere, the plasma sheet appeared to be bent at about $X = -10$ R_E. P3 and P4 were next to the bending point. The AM-03 model suggested that just three minutes later (at 7:23 UT), a thin current sheet formed at the plasma sheet bending point, as shown in the third panel in Figure 5. This magnetotail configuration appeared to be quasi-stable until 7:34 UT, when the plasma sheet started to slowly dipolarize. We show one snapshot of the gradual plasma sheet dipolarization process in Figure 5, fourth panel. At 7:38 UT the snapshot appeared to be the final stage of the slower plasma sheet dipolarization; a much faster magnetotail dipolarization was detected at 7:39 UT, as shown in the fifth panel of Figure 5. We also draw one field line in all panels of Figure 5 in red. The red field line has foot points always at the same latitude. During the fast dipolarization it moved about 5 R_E Earthward within one minute.

[22] Figure 6 (top) shows the location of the neutral sheet according to the AM-03 model for the midnight meridian $(X, Z)_{GSM}$ plane before (7:00 UT, red curve) and after (7:21 UT, green curve) the abrupt bending. After 7:21 UT the neutral sheet tailward of the bending point (point with the largest curvature) was always between the green and the blue (7:35 UT) curves. Figure 6 (bottom) shows the cross-tail current density at the neutral sheet according to the AM-03 model for the midnight meridian depending on the X_{GSM} coordinate. At 7:00 UT, before the

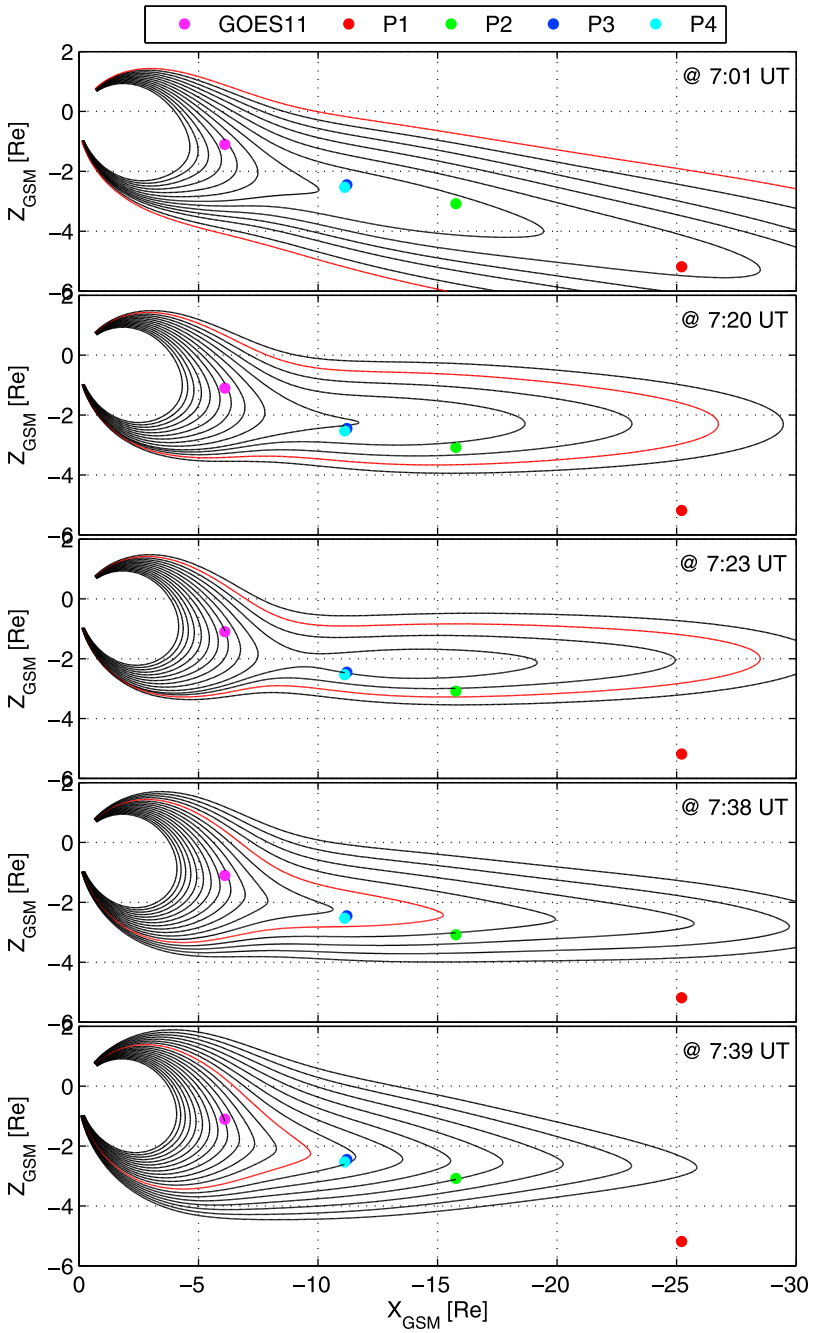

Figure 5. Magnetic field lines according to the AM-03 model shown in the noon meridian GSM plane on 28 February 2008 at 7:01 UT, 7:20 UT, 7:23 UT, 7:38 UT, and 7:39 UT. Locations of the P1–P4 THEMIS and GOES 11 spacecraft are overplotted (see legend for color coding). The red line in all panels stems from the same latitude.

abrupt bending the current density was smaller at all distances; it reached a maximum at around $X_{GSM} = -6\ R_E$. After the abrupt bending (after 7:21 UT), the current density grew and the maximum moved from -6 to $-10\ R_E$. Maximal current densities were predicted between 7:35 and 7:40 UT. Temporal evolution of the neutral sheet location and current density for all times between 6:50 and 7:50 UT are shown in Figure A2. One can see that the original plasma sheet was bent only slightly, with the bending point located around $X_{GSM} = -7\ R_E$ and an about 7 degree bending angle. The abrupt bending between 7:10 and 7:20 UT moved the bending point more tailward (at about $-9\ R_E$) and increased the bending angle to about 15 degrees. The current density started to increase immediately after the bending.

2.2. Evolution of Magnetic Field and Pressure Gradients Near the Bending Point

[23] In order to provide the overall magnetospheric context, we present OMNI 1 min IMF and plasma data in Figure 7. One can see that the IMF B_Z remained positive

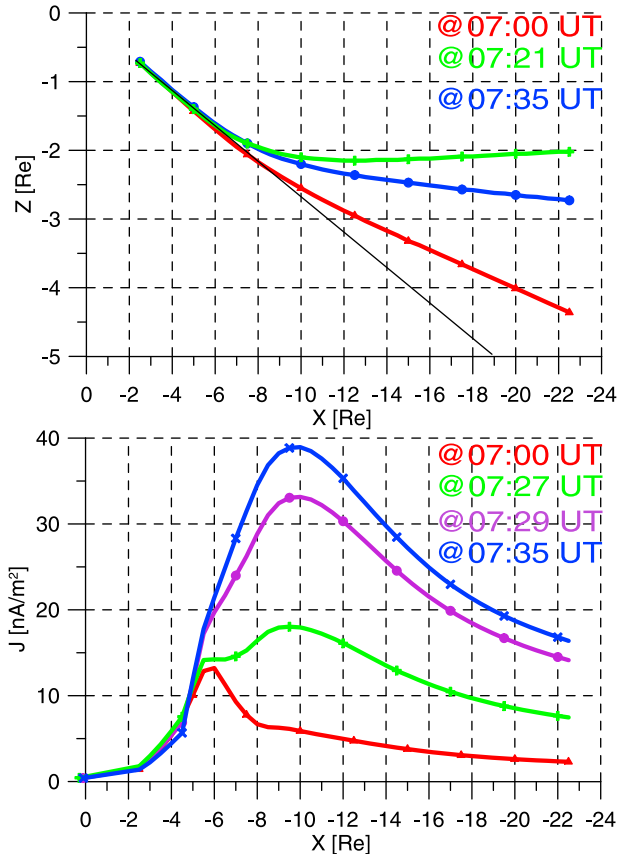

Figure 6. (top) Z_{GSM} coordinate of the neutral sheet and (bottom) cross-tail current density at the neutral sheet according to the AM-03 model for the midnight meridian as a function of the X_{GSM} coordinate on 28 February 2008 at different times between 7:00 UT (red) and 7:37 UT (blue). In the top panel we also plot a straight (black) line perpendicular to the magnetic dipole in order to estimate the bending angle of the magnetotail. See legends for color coding and text for details.

(between 1 and 3 nT) after 7:04 UT. Also, no sharp increases in the ion velocity and density were observed, suggesting a stable dynamic pressure of about 1.8 nPa (not shown here). The *Dst* index was about −18 nT, and the auroral indices showed rather small activity.

[24] In Figure 8a we plot the lobe magnetic field, estimated using the AM-03 model. The magnetic field in the lobes did not grow. On the contrary, a slight decline can be seen. We therefore conclude that the above shown plasma sheet thinning was not forced by an increase in magnetic pressure in the lobes, which is in agreement with the solar wind data in Figure 7. We note, however, that rather small values of B_Z between 40 and 45 nT observed by GOES 11 at the geostationary orbit suggest that the magnetotail was already in a somewhat loaded condition.

[25] Figure 8b shows the evolution of total pressure gradient along the X_{GSM} axis. Figures 8c and 8d demonstrate the evolution of the gradients of the Z_{GSM} component of the magnetic field B_Z along the X_{GSM} axis (Figure 8c) and along the Y_{GSM} axis (Figure 8d).

[26] The gradients were calculated using data from P2, P3, and P4, which were located between $X = -11$ R_E and $X = -16$ R_E, near the bending point. To obtain the gradients along the X_{GSM} direction, we calculated differences in total pressure and B_Z between P2 and P3 and between P2 and P4 and divided them by the distances between the probe pairs along the X_{GSM} axis (cf. Figures 8b and 8c). To obtain the gradient along the Y_{GSM} direction, we calculated differences in B_Z between P3 and P4 and divided them by the distance between P3 and P4, which was more than five times shorter than the distance between the P2–P3 and P2–P4 pairs along the X_{GSM} axis (cf. Figure 8d). This does not allow us to directly compare the absolute values of the gradients along the X_{GSM} and Y_{GSM} axes.

[27] The total pressure gradient was roughly constant until about 7:30 UT, when it started to decrease rapidly toward reconnection time, 7:39 UT. In contrast, $\partial B_Z/\partial X$ was closer to zero between 6:50 and 7:10 UT. After plasma sheet bending (after 7:10 UT), $\partial B_Z/\partial X$ gradually became more negative until 7:30 UT. Between 7:30 and 7:36 UT, it did not change significantly. Then at 7:36 UT it rapidly returned to zero again. Such observations suggest that between 7:30 and 7:36 UT, the plasma sheet started gradually embedding [*Petrukovich et al.*, 2007]; i.e., the current sheet profile became thinner than the plasma sheet [*Artemyev et al.*, 2010; *Petrukovich et al.*, 2011]. After reconnection (at 7:40 UT) $\partial B_Z/\partial X$ became strongly positive. One can see that it reached down to -1 nT/R_E. We note that this is an average value of the gradient over distances between P2 and P3/P4 of the order of 5 R_E. We also show the temporal evolution of B_Z for all times between 6:50 and 7:50 UT in Figure A3.

[28] We plot $\partial B_Z/\partial X$ in the GSM frame of reference (black curves in Figure 8d) and local neutral sheet coordinates as predicted by the AM-03 model (blue curves in Figure 8d).

[29] Similarly, we investigated the evolution of total pressure gradients and the Z component of the magnetic field Z_{GSM} along the Y_{GSM} axis, which also tended to vanish between 7:36 and 7:38 UT, immediately before reconnection.

3. Wave Mode Identification

[30] In this section we investigate the magnetic field oscillations shown in Figure 1 in more detail with the help of Figures 9–15.

[31] Using only magnetic field and ion density observations, *Du et al.* [2011] interpreted the oscillations detected by P3 and P4 as compression waves. Here we further analyze these oscillations with the help of the electric field and electron distribution functions.

[32] Changes in the B_X component of the magnetic field are often associated with plasma sheet flapping [see, e.g., *Zhang et al.*, 2002; *Runov et al.*, 2005; *Sergeev et al.*, 2006; *Petrukovich et al.*, 2006, 2008; *Runov et al.*, 2009, and references therein]. The signature of vertical motion is correlation of the time derivative of the X_{GSM} component of the magnetic field $\partial B_X/\partial t$ with the Z_{GSM} component of the plasma velocity. Unfortunately, as one can see in Figure 2, the velocity measurements were too noisy to make such an analysis with the help of the plasma spectrometers. We, however, were able to derive the Z_{GSM} component of the

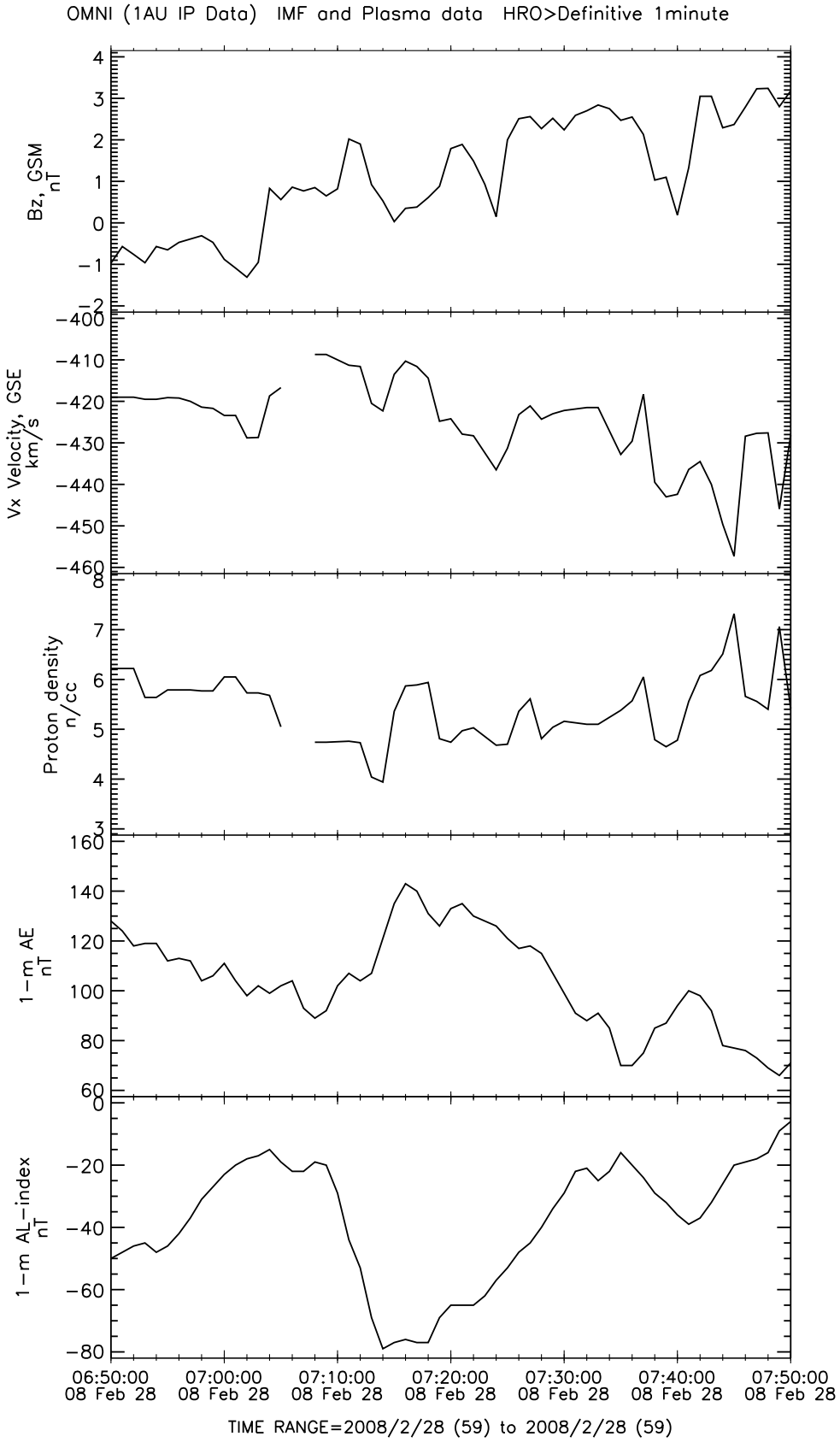

Figure 7. OMNI 1 minute IMF and plasma data showing (top to bottom) the *Z* component of the interplanetary magnetic field, the *X* component of the solar wind velocity, the solar wind density, and AE and AL indices at 1 AU on 28 February 2008 between 6:50 and 7:50 UT.

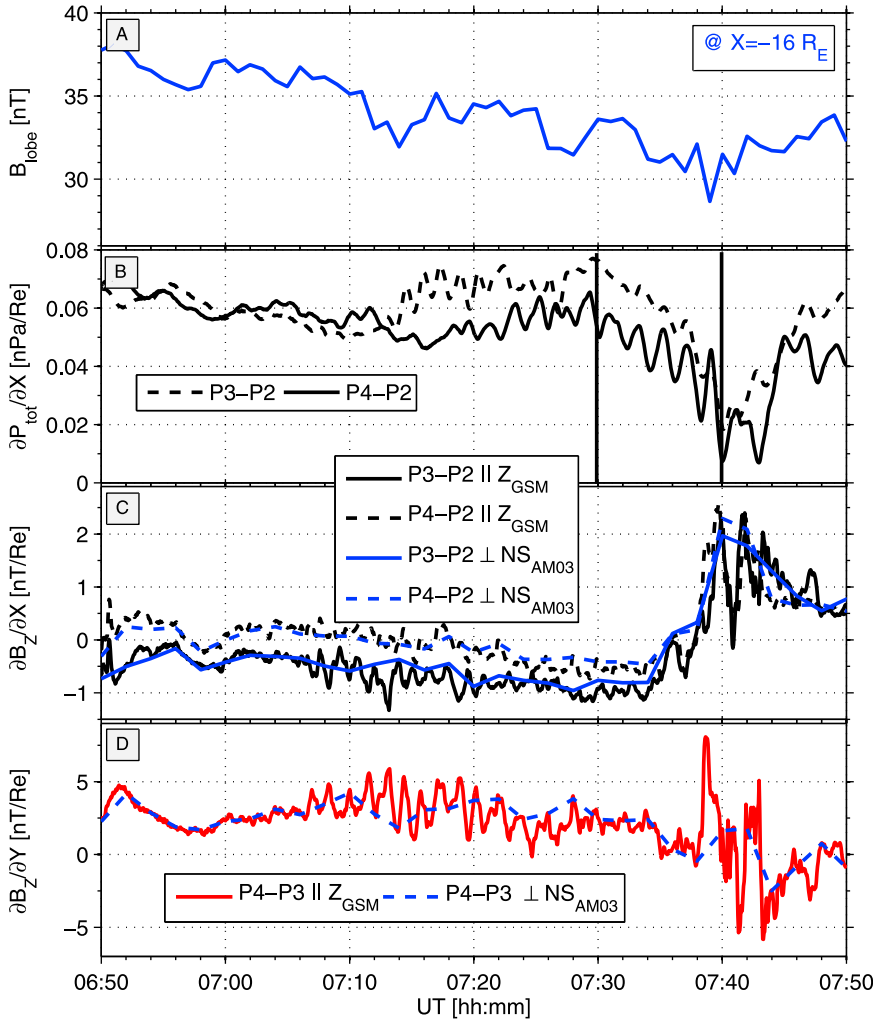

Figure 8. Data from THEMIS probes on 28 February 2008 between 6:50 and 7:50 UT. (a) Magnetic field in lobes estimated using the AM-03 model for $X = -16$ R_E; (b) radial pressure gradient $\partial P/\partial X$ between P3 and P2, dashed curve, and between P4 and P2, solid curve; (c) radial gradient of the Z_{GSM} component of the magnetic field $\partial B_Z/\partial X$ between P3 and P2, dashed curves, and between P4 and P2, solid curves; and (d) transverse gradient of the Z_{GSM} component of the magnetic field $\partial B_Z/\partial Y$ between P4 and P3. The blue lines in Figures 8c and 8d show the corresponding gradients of the magnetic field component perpendicular to the neutral sheet plane as predicted by the AM-03 model in the top panel of Figure 6. See legends for color coding.

convection velocity from the more accurate electric field measurements and show it in Figure 9 (bottom) for P4 on 28 February 2008 between 7:01 and 7:05 UT. Indeed, $-(\mathbf{E} \times \mathbf{B}/B^2)_Z$ was positive during the steep B_X increases. Also $-(\mathbf{E} \times \mathbf{B}/B^2)_Z$ was negative (nearly vanished) during steeper (nearly flat) decreases. For better visibility, in Figure 9 (bottom) we also overplot the time derivative of the X component of the magnetic field multiplied by ten, which appears to be in phase with $-(\mathbf{E} \times \mathbf{B}/B^2)_Z$. During this time interval the oscillation amplitudes in B_X did not exceed 3 nT. In turn, $(\mathbf{E} \times \mathbf{B}/B^2)_Z$ was extremely small, less than several km/s. We note that plasma sheet bending was weaker; it did not exceed 7 degrees.

[33] The first two panels in Figure 10 show similar data for P4 between 7:13 and 7:23 UT, during the abrupt increase in the bending angle. The oscillation amplitude simultaneously grew several times (up to 10 nT), as did $(\mathbf{E} \times \mathbf{B}/B^2)_Z$ (up to 20 km/s).

3.1. Kinetic Ballooning/Interchange Instability Signatures

[34] The above continuous observation of flapping signatures could agree with drift-kink [*Lapenta and Brackbill*, 1997; *Daughton*, 1999; *Karimabadi et al.*, 2003a, 2003b; *Zelenyi et al.*, 2009] and double-gradient instability [e.g., *Erkaev et al.*, 2008; *Korovinskiy et al.*, 2011] theories. The drift-kink instability does not, however, explain the complementary, significant in-phase oscillations of the Z_{GSM} component of the magnetic field shown in the third panel of Figure 10.

[35] Oscillations of B_Z characterize, for example, the ballooning/interchange instability [*Pritchett and Coroniti*, 2010, 2011]. In Figure 5 of *Pritchett and Coroniti* [2010]

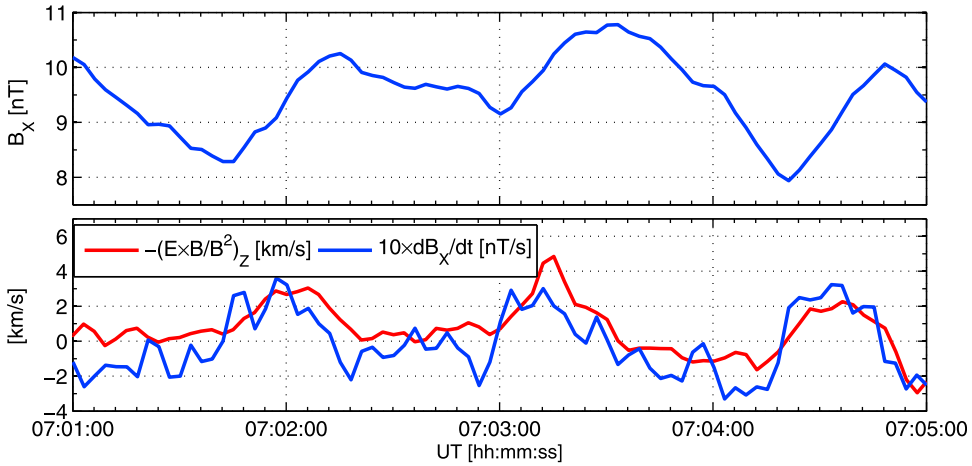

Figure 9. (top) X_{GSM} component of the magnetic field and (bottom) Z_{GSM} component of the **E** × **B**-drift velocity and time derivative of the X_{GSM} component of the magnetic field multiplied by 10, as measured by P4 on 28 February 2008 between 7:01 and 7:05 UT. See legend for color coding.

B_Z increases correspond to elongated structures—ballooning/interchange fingers. In spacecraft observations these oscillations can also appear from B_X oscillations in a tilted plasma sheet. However, the results of the AM-03 model have suggested that after 7:20 UT the plasma sheet was nearly horizontal downtail from the bending point. The plasma velocities associated with ballooning/interchange instability fingers are shown in *Pritchett and Coroniti* [2010, Figures 6 and 7]. The fourth and fifth panels in Figure 10 of our paper are plotted in the same layout as Figure 7 in *Pritchett and Coroniti* [2010]. One can indeed see that the X_{GSM} component of the electron velocity is correlated with B_Z oscillations. Also, the amplitudes of the electron velocity oscillations are substantially larger than those of the ion velocity.

[36] The sawtooth structure of the magnetic field oscillations can be seen, e.g., in the first panel of Figure 10. It is accompanied by narrow, fast, Earthward electron flows that are interlaced with the wider, slower, tailward flowing electrons. A similar picture characterizing the development of ballooning/interchange fingers can be found in *Pritchett and Coroniti* [2011, Figures 2 and 4].

[37] Figure 11 (top) shows the X_{GSM} component of the electron velocity divided by 500 (blue) and the time derivative of the Z_{GSM} component of the magnetic field (magenta) from P4 between 7:10 and 7:30 UT. With the help of linearized electron fluid equations, we found that $\partial B_Z/\partial t$ should be proportional to the electron velocity with the coefficient of proportionality equal to $-\partial B_Z/\partial X$ (see Appendix B for details). Figure 11 (bottom) shows the cross-correlation coefficient of the curves in the top panel, which depends on the time shift for the original signals and for the signals filtered near 10 mHz. The highest correlation maximum can be indeed found near zero time shift.

[38] One can also see from Figure 11 that $\partial B_Z/\partial X$ was approximately equal to $-1/500$ nT/km. This means that $\partial B_Z/\partial X$ at P4 was 1 order of magnitude stronger than what we obtained in Figure 8 as a value averaged through radial distances between 11 and 16 R_E downtail.

3.2. Cross-Tail Drift of the Ballooning/Interchange Fingers

[39] The significant separation of P3 and P4 only along the Y_{GSM} axis made it possible for us to estimate the propagation velocity in the cross-tail direction. As one can see from Figure 1, the X_{GSM} component of the magnetic field is dominant for the observed oscillations. The measurements of P2 and P3 provided a better similarity in the Z_{GSM} component of the magnetic field, however. This can be seen in Figure 12, which demonstrates the X_{GSM} and Z_{GSM} components of the magnetic field measured by P2, P3, P4, and GOES 11. Figure 13 shows the cross-correlation coefficient of the Z_{GSM} component of the magnetic field measured by P3 and P4 between 7:13 and 7:33 UT. The cross-correlation maximum at the time shift about 50 s suggests that the ballooning/interchange fingers propagated parallel to the Y_{GSM} axis at a speed of about 100 km/s. Taking into account the latter estimate and recalling from Figure 10 that the time duration of the positive electron peaks was on the order of 20 s, we obtain a half width of the ballooning/interchange fingers of about 2000 km or about ten proton gyroradii in the lobes.

3.3. Sausage-like Structure of the Ballooning/Interchange Fingers

[40] In Figure 14 (top) we plot the X component of the magnetic field at P3 and P4. The data from P4 was shifted by 50 s, as defined by the cross-tail propagation velocity which was obtained in section 3.2. The cross spectrum of the two signals in Figure 14 (middle) shows maximum around the scales of 40 s, which is about a half period of the observed oscillations in the X component of the magnetic field at P3 and P4. Figure 14 (bottom) shows the phase shift between the two signals as a function of time. Because of the 50 s shifting of the P4 data the phase shift between 7:13 and 7:33 UT is close to zero. We note that during this time interval both P3 and P4 observed largely negative values of B_X, and therefore were located southward from the neutral sheet. Between about 7:07 and 7:13 UT the spacecraft were located in different hemispheres, and the phase shift was about 180 degrees. This observation suggests that the oscillations have a sausage-like

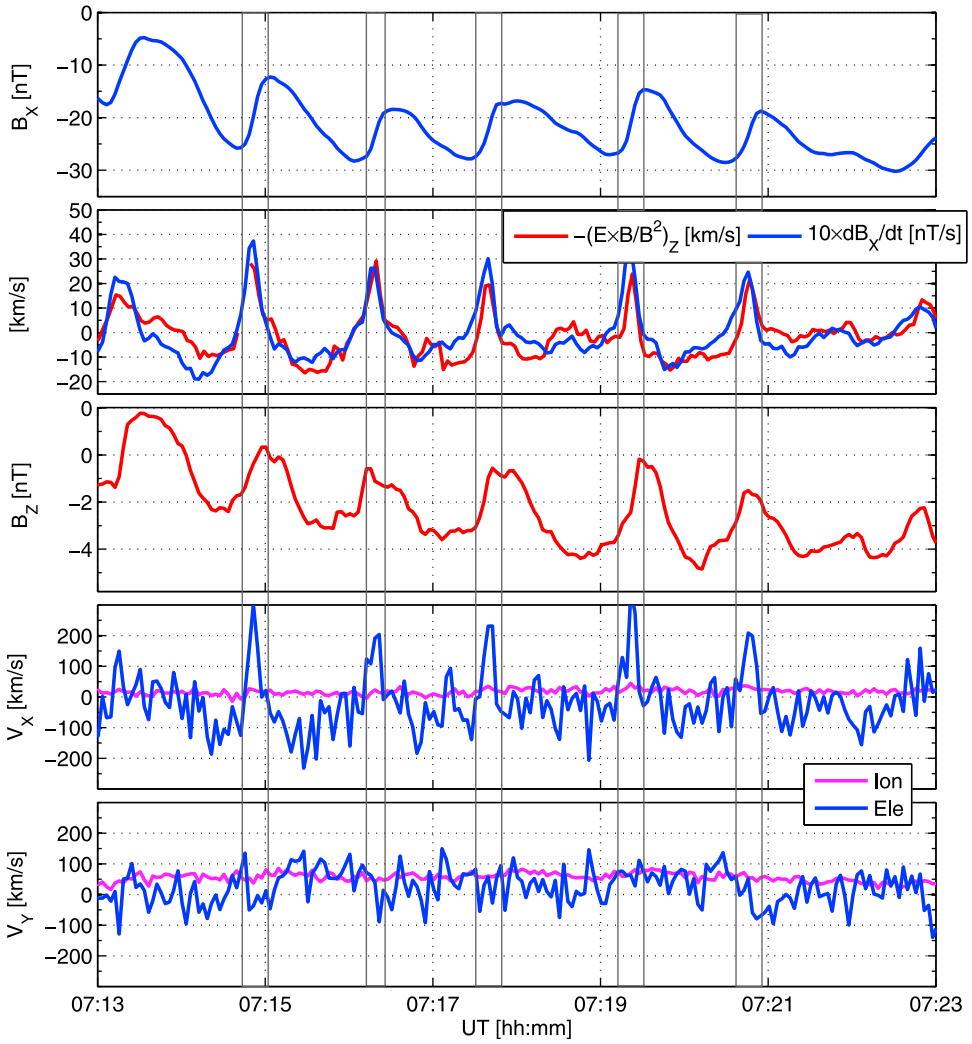

Figure 10. From top to bottom are shown X_{GSM} component of the magnetic field, Z_{GSM} component of the **E** × **B**-drift velocity (red) and time derivative of the X_{GSM} component of the magnetic field multiplied by 10 (blue), Z_{GSM} component of the magnetic field, X_{GSM}, and Y_{GSM} components of the ion velocity (magenta) and the electron velocity (blue) measured by P4 on 28 February 2008 between 7:13 and 7:23 UT. See legends for color coding.

structure when the spacecraft observed interlaced thickening and shrinking of the plasma sheet.

3.4. Elongation of the Ballooning/Interchange Fingers

[41] After 7:30 UT, P2 at 16 R_E downtail and GOES 11 at 6 R_E downtail started to observe oscillations similar to those demonstrated above for P3 and P4. We show these oscillations in Figure 15 (see legend for color coding). Simultaneous observation of the ballooning/interchange fingers by P2, P3, P4, and GOES 11 suggests that the ballooning/interchange fingers were at this moment at least 10 Earth radii long. Therefore, the length-to-width ratio of the ballooning/interchange fingers appeared to be over twenty.

[42] The oscillations' amplitude in B_Z at P2 (green curve in Figure 15a) increased from period to period, as did the time derivative of the Z_{GSM} component of the magnetic field (cf. Figure 15b). Although such growth was not clearly observed in the magnetic field oscillations at P3 (blue curve in Figure 15a), we noticed a similar growth in other plasma parameters at both P2 and P3. For example, the oscillations' amplitude in $(\mathbf{E} \times \mathbf{B}/B^2)_Z$ (Figure 15c) and the X_{GSM} component of the plasma velocity (Figure 15d) grew, as well.

[43] *Pritchett and Coroniti* [2011] demonstrated that the ion bulk velocity oscillation amplitude along the X direction V_{ix} at later times (at $\Omega_{i0}t = 56$) grew to a substantial fraction of the ion thermal velocity V_T (note that the x axis in the simulations by *Pritchett and Coroniti* [2011] points tailward). In addition, Figure 4 of *Pritchett and Coroniti* [2011] shows that V_{ix} oscillations are in-phase with the oscillations of the logarithm of plasma density. At P3 the amplitude of the ion velocity oscillations exceeded the noise level, which allowed us to directly check for a correlation between V_X and the plasma density (the plasma density, not shown here, was correlated with the total pressure oscillations shown by the blue curve in Figure 15h; see also the third and fourth panels in Figure A1). Indeed, in our observations, V_X (Figure 15d) appeared to anticorrelate with the total pressure (and the density) oscillations.

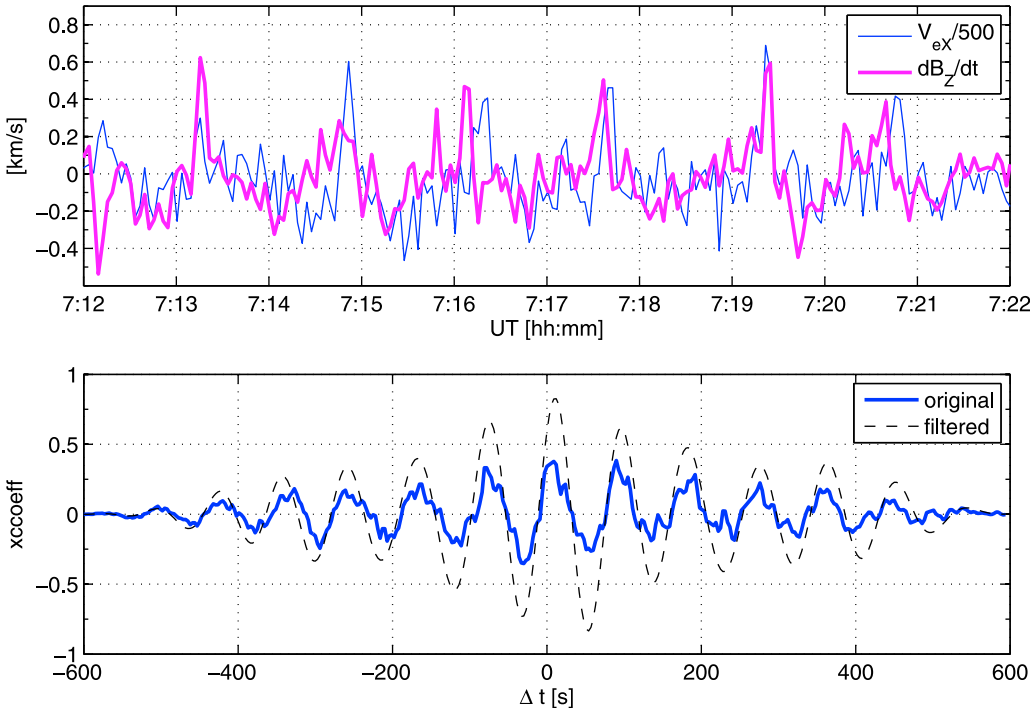

Figure 11. (top) X_{GSM} component of the electron velocity divided by 500 (blue) and the time derivative of the Z_{GSM} component of the magnetic field (magenta) measured by P4 on 28 February 2008 between 7:12 and 7:22 UT. (bottom) Cross-correlation coefficient of the curves in the top panel for different time shifts between the original signals and signals filtered near 1/100 Hz.

[44] Growth of the ion velocity in the Y_{GSM} direction (cf. Figure 15e) suggests increase in the cross-tail current. Indeed, this observation agrees with the current increase predicted by the AM-03 model, shown in Figure 15f (see also Figure A2). The cross-tail current grew especially strongly between 8 and 13 R_E (cf. Figure A2b); i.e., around the location of P3 and when the total pressure gradient decreased (Figure 15g). Although the total pressure gradient decreased, the oscillations' amplitude of total pressure at P2 and P4 increased (Figure 15h). Finally, at about 7:38 UT the radial gradient of the Z_{GSM} component of the magnetic field vanished (Figure 15i). At this point the plasma sheet at radial distances between 11 and 16 R_E appeared to be a nearly one-dimensional thin current sheet. It is worth noting that the current wedge on the ground started to form already between 7:30 and 7:34 UT, as can be seen from Figure 15j. The details of current wedge formation during this event will be reported elsewhere.

4. Summary and Discussion

[45] In this paper we studied the observations of the THEMIS and GOES 11 probes on 28 February 2008 between 6:50 and 7:50 UT. During this period we tracked plasma sheet bending (presumably) by the solar wind. Immediately after bending it started embedding and finally dipolarized after magnetotail reconnection, which was initiated in the thinnest part of the plasma sheet at $-16 < X < -11$ R_E.

[46] AM-03 model calculations suggested that plasma sheet embedding and subsequent reconnection were not caused by increased magnetic flux in the lobes. Instead, we found that after bending, the gradient $\partial B_Z/\partial X$ turned negative and the plasma sheet exhibited strong oscillations.

[47] Theory predicts that a plasma sheet configuration with negative $\partial B_Z/\partial X$ may be unstable for both a double-gradient instability [*Erkaev et al.*, 2008; *Korovinskiy et al.*, 2011] and a ballooning/interchange instability [*Pritchett and Coroniti*, 2010]. While the former generates plasma sheet flapping oscillations, the latter is responsible for the formation of sausage-like fingers. Both types of disturbances would propagate in the direction of the ion bulk flow.

[48] We found several signatures indicating that the studied oscillations began during the development of kinetic ballooning/interchange instability: (1) correlation of the vertical velocity and $\partial B_X/\partial t$, (2) strong oscillations of B_Z, (3) in-phase oscillations in B_X and B_Z, (4) sausage-like structure, (5) strong oscillations of the total pressure, (6) fast periodical electron flows, (7) oscillation frequency about 0.01 Hz, (8) propagation at a velocity of about 100 km/s in Y_{GSM}, and (9) fingers' half width about 2000 km.

[49] The three last parameters are in quantitative agreement with the theoretical predictions of *Pritchett and Coroniti* [2010]. In particular, they estimated that the real frequency is about 60% of the ion cyclotron frequency at the neutral sheet. In our case this frequency was between 0.01 and 0.02 Hz (for B_Z between 2 and 1 nT). *Pritchett and Coroniti* [2010] also estimated the propagation velocity of the instability fingers in the Y direction as an ion drift speed multiplied by the ratio between the oscillation frequency and the ion gyrofrequency in the neutral sheet. This ratio was about unity in our observations, suggesting 100 km/s (or one

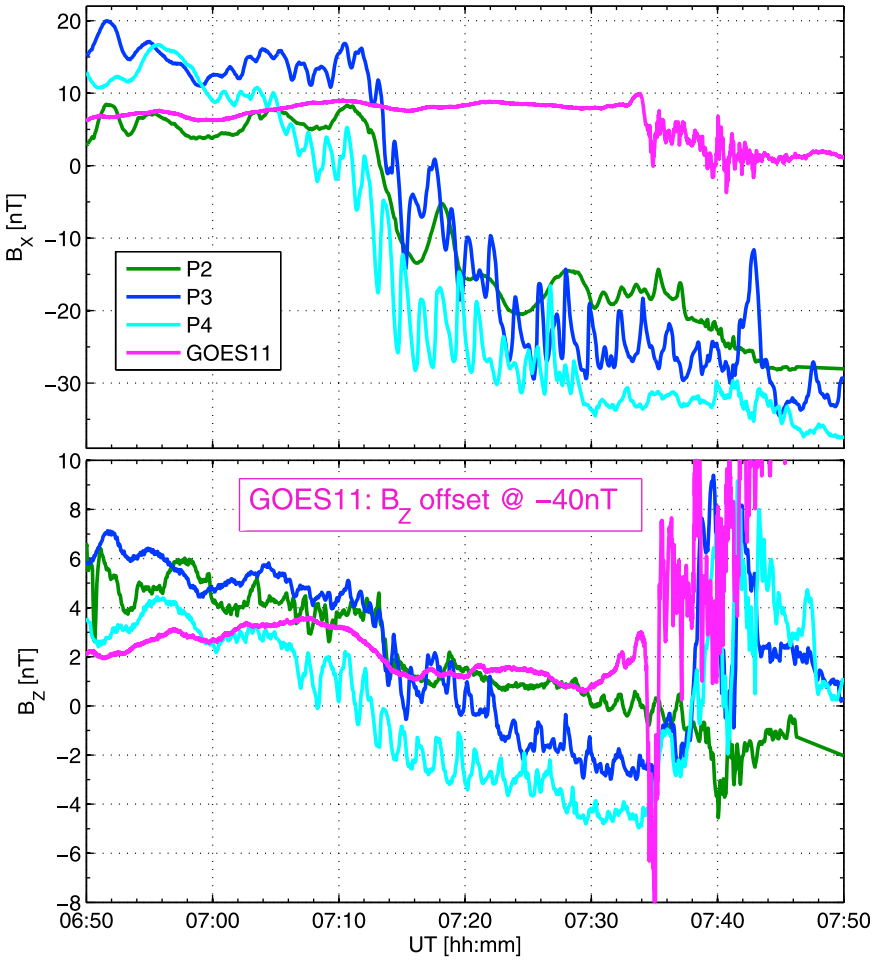

Figure 12. X_{GSM} and Z_{GSM} components of the magnetic field measured by P2, P3, and P4 on 28 February 2008 between 6:50 and 7:50 UT.

ion drift speed) propagation velocity in the y direction, which appeared exactly equal to the estimates made using the above THEMIS observations.

[50] We note that earlier attempts to take into account kinetics for the development of a ballooning/interchange instability were made by *Cheng and Lui* [1998]. Indications for the development of a ballooning/interchange instability were recently suggested by *Liang et al.* [2008] and *Saito et al.* [2008]. The MHD calculations of *Cheng and Lui* [1998] were constrained by finite ion gyroradius effects in a high-β plasma sheet. The remarkable agreement of electron flows with the full PIC modeling by *Pritchett and Coroniti* [2010] have shown that electron kinetics should not be neglected, however.

[51] The plasma sheet started to exhibit sausage-like oscillations near the bending point at $X_{GSM} = -11\ R_E$. The amplitude of the oscillations grew substantially with larger bending angles after 7:10 UT. The value of $\partial B_Z/\partial X$ continued its negative growth until 7:30 UT. At 7:30 UT THEMIS and GOES 11 detected that the oscillation region extended in both directions from $X_{GSM} = -11\ R_E$ (to $-6\ R_E$ and $-16\ R_E$); i.e., the length of the ballooning/interchange fingers along the X_{GSM} axis exceeded 10 R_E.

[52] When the length-to-width ratio of the ballooning/interchange finger reaches a critical value, the ballooning/interchange instability can become linearly unstable—the instability will grow infinitely during a finite time. Such a critical value was introduced by *Hurricane et al.* [1999]: $\xi_\psi/L \approx \tau_A^2(\omega_{*i}^2/4 - \Gamma^2)$, where the radial plasma displacement ξ_ψ can be taken equal to the finger length, the equilibrium scale length L can be taken equal to the finger width, the Alfvén time τ_A is on the order of hundreds of seconds, the diamagnetic drift frequency $\omega_{*i} = k_\perp v_{iondrift}$ is on the order of 0.1 Hz, and the growth rate Γ for the ballooning/interchange mode is negative below marginal stability.

[53] Indeed, in Figure 15 we see consequent growth of the ballooning/interchange instability in several plasma and magnetic field parameters. After fewer than ten periods of stable growth, current sheet reconnection was observed, as shown in Figure 3. The observed reconnection during the nonlinear stage of ballooning/interchange instability development was predicted in terms of a 'substorm detonation' [*Hurricane et al.*, 1999]. In our observations substorm detonation was expected for the values of ξ_ψ/L above the order of 10. Indeed, we found that the length-to-width ratio of the observed ballooning/interchange fingers exceeded 20 (the distance between

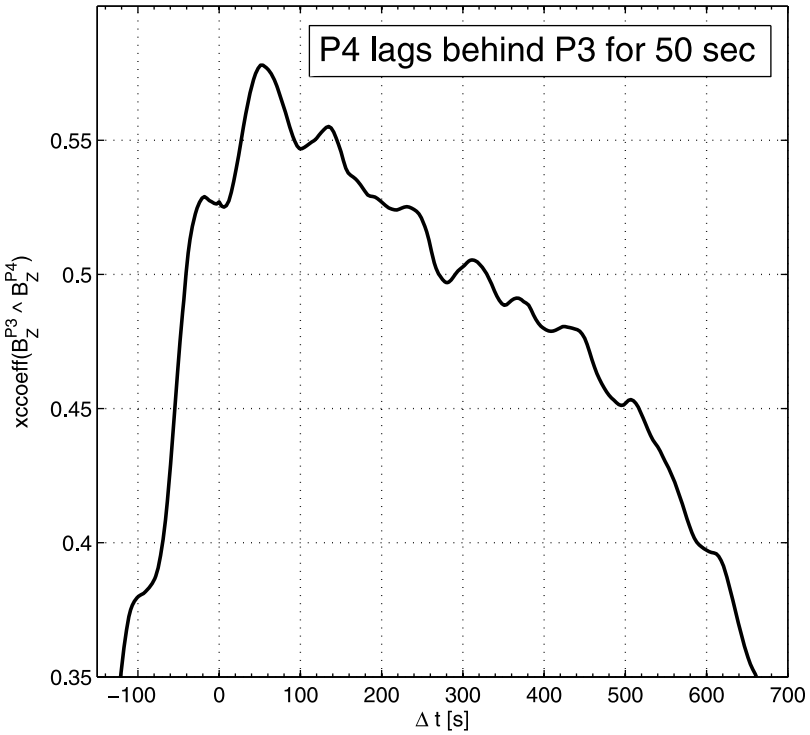

Figure 13. Cross-correlation coefficient of the Z_{GSM} component of the magnetic field measured by P3 and P4 on 28 February 2008 between 7:13 and 7:33 UT. See text for details.

GOES 11 was about 10 R_E, whereas the half width of the ballooning/interchange fingers appeared to be about 2000 km).

[54] Recent numerical modeling has also confirmed that current sheet reconnection may result from development of a ballooning/interchange instability *Pritchett and Coroniti* [2011]. And several reconnection signatures were seen both in our observations and in the simulations by *Pritchett and Coroniti* [2011]. For instance, the difference between reconnection flow observations at P3 and P4 suggests that the flow

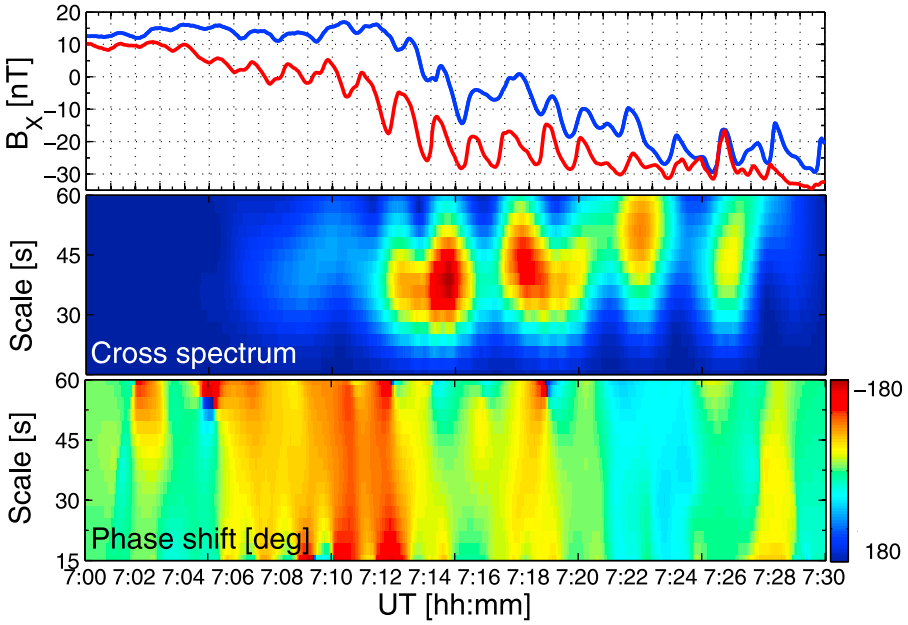

Figure 14. (top) B_X component of the magnetic field at P3 and P4 on 28 February 2008 between 7:00 and 7:30 UT, (middle) wavelet cross-correlation coefficient plotted using the signals from the top panel, and (bottom) phase shift in the oscillations of the two signals.

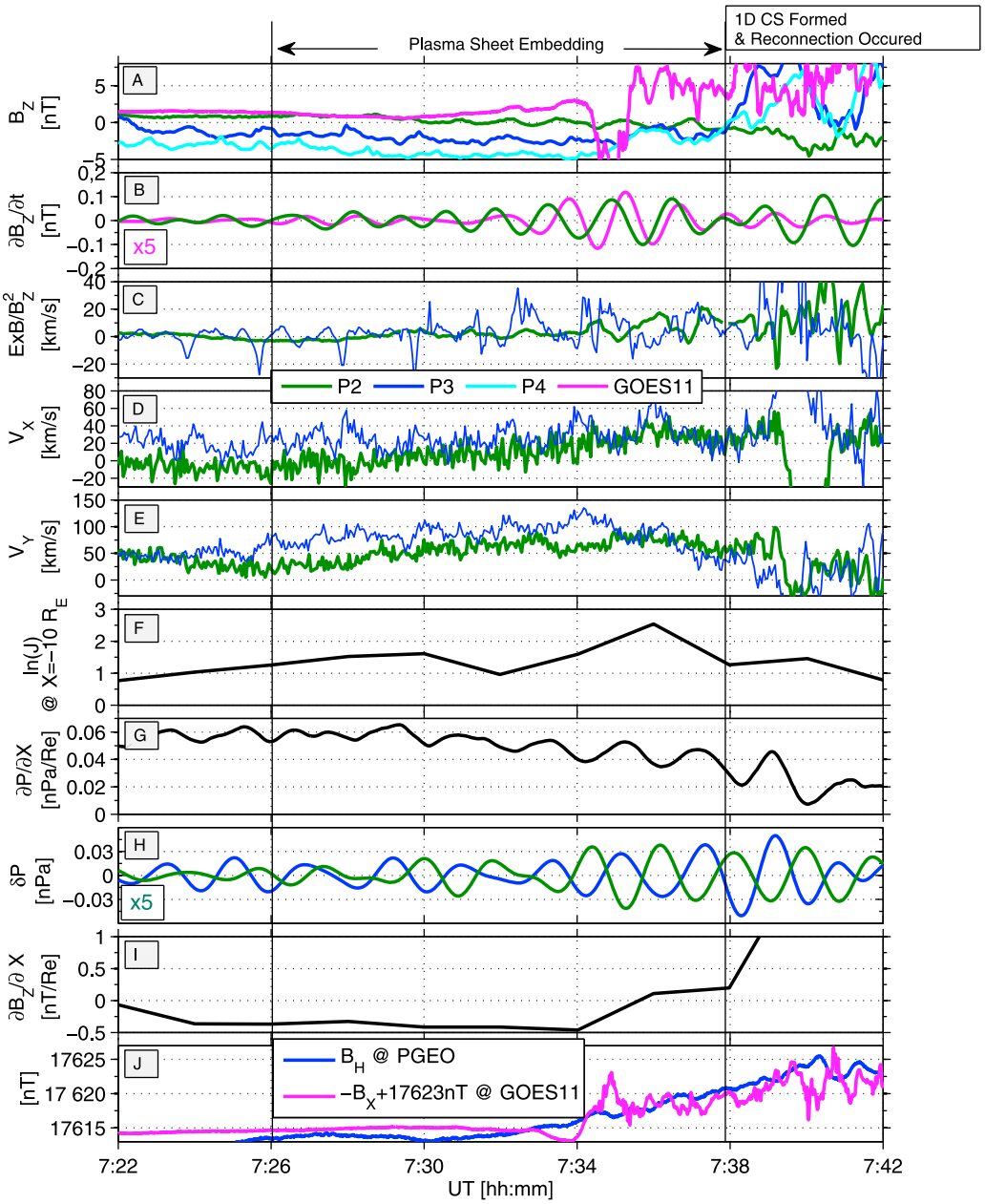

Figure 15. (a) Z_{GSM} component of the magnetic field; (b) time derivative of the Z_{GSM} component of the magnetic field bypass filtered between 1 and 10 mHz (at GOES 11 (magenta) multiplied by a factor of 5 for better visibility); (c) Z_{GSM} component of the **E** × **B**-drift velocity; (d) X_{GSM} and (e) Y_{GSM} components of the ion velocity; (f) natural logarithm of the current density at the neutral sheet at X_{GSM} = −10 R_E, according to the AM-03 model;(g) radial pressure gradient $\partial P/\partial X$ between P2 and P3; (h) oscillations' amplitude in the total pressure bypass filtered between 1 and 10 mHz (at P2 (green) multiplied by a factor of 5 for better visibility); (i) radial gradient $\partial B_Z/\partial X$ between P2 and P3; and (j) B_H component of the magnetic field measured by the ground-based magnetometer at Prince George (Canada) with overplotted profile of $-B_X$ + 17623 nT from GOES 11 on 28 February 2008 between 7:10 and 7:40 UT. See legends for color coding.

channel was narrow or curved, which is in agreement with *Pritchett and Coroniti* [2011, Figure 3].

[55] In addition, theoretical works indicate that the reconnection observed by THEMIS and in the simulations by *Pritchett and Coroniti* [2011] may have been caused during ballooning/interchange instability development. *Yang et al.* [2011] and *Hu et al.* [2011] used MHD simulations to investigate the evolution of a plasma sheet in which a bubble-blob pair was artificially set. The result of the study was, in particular, accelerated thinning of the plasma sheet and consequent reconnection.

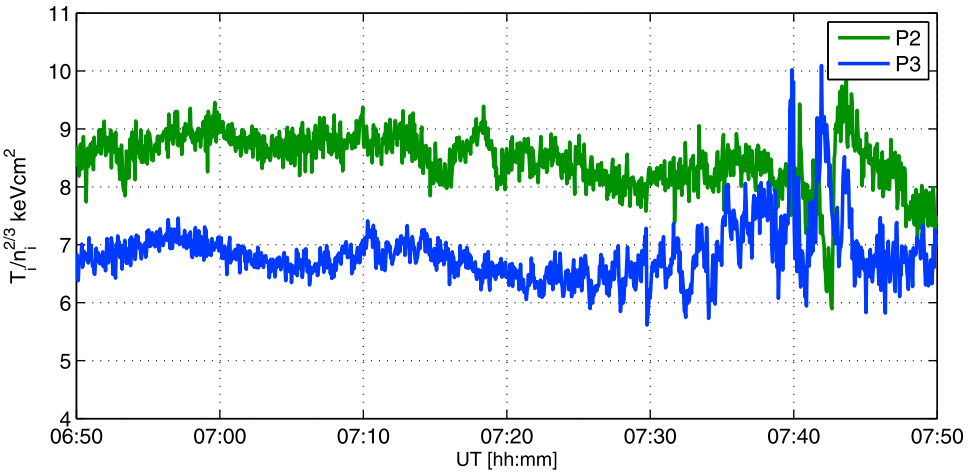

Figure 16. Value of $T/n_i^{2/3}$ from THEMIS P2 (green) and P3 (blue) on 28 February 2008 between 6:50 and 7:50 UT.

[56] Figure 16 shows values of $T/n_i^{2/3}$ for P2 (green) and P3 (blue). The logarithm of $T/n_i^{2/3}$ is expected to be inversely proportional to the local value of entropy. After 7:30 UT P3 started to observe ballooning/interchange fingers with more and more depleted entropy. At 7:37 UT, immediately before reconnection, the entropy in the ballooning/interchange fingers at P3 reached the same values as observed by P2. Figure 17 provides a possible interpretation of the observations in Figure 16 that is consistent with the results of *Yang et al.* [2011] and *Hu et al.* [2011]. The bottom of Figure 17 shows the radial profile of B_Z; a minimum is the point with $\partial B_Z/\partial X = 0$. We suggest that the ballooning/interchange fingers A and B were located at least partly to the right of the point with $\partial B_Z/\partial X = 0$. When the next finger became fully located Earthward from the point with $\partial B_Z/\partial X = 0$, the buoyancy force started to pull it (with lower entropy and larger B_Z) further Earthward, while the conjugated space between the fingers (with higher entropy and lower B_Z) was pulled tailward toward the point with $\partial B_Z/\partial X = 0$. Such a configuration is similar to those in simulations of the bubble-blob pair interaction, which, according to *Yang et al.* [2011] and *Hu et al.* [2011], would lead to local reconnection.

[57] We do not exclude the possibility that the ballooning/interchange instability only preconditions a magnetotail geometry that would be favorable for reconnection. For example, complex dynamics of the ballooning/interchange fingers may produce a finite amplitude tearing perturbation of sufficient strength to locally reverse the normal component, create alternating X-type neutral lines, and produce a so-called hard onset of tearing instability [*Galeev et al.*, 1985]. Alternately, the tearing instability may be initiated by the negative $\partial B_Z/\partial X$ [*Sitnov and Schindler*, 2010]. The possibility of normal reconnection after some reconnection-preconditioning process was considered, by, e.g., *Nakamura et al.* [2011]. They suggested that a preceding reconnection took the magnetic flux away and created a second diffusion region, provoking another reconnection. Because of the complex three-dimensional geometry, however, it is expected that the dissipation mechanism for reconnection that occurs during ballooning/interchange instability development may be different from theories in which simpler current sheet configurations were considered [e.g., *Fujimoto*, 2011].

[58] Note that reconnection was observed during magnetotail embedding, which is usually associated with the substorm growth phase, [e.g., *Petrukovich et al.*, 2007; *Artemyev et al.*, 2010; *Petrukovich et al.*, 2011]. Indeed, simultaneously with reconnection, at the foot points of the field lines leading to the THEMIS probes, the THEMIS all-sky camera array observed a substorm breakup arc (not shown here), which manifested the substorm expansion phase. One should note that the substorms during the northward IMF, the so-called contracted oval substorms, are systematically observed. They are characterized by lower geomagnetic activity and longer ionospheric response time [e.g., *Petrukovich et al.*, 2000].

[59] Observations have also revealed flapping oscillations during the growth phase of a substorm [*Runov et al.*, 2009]. Indeed, other theoretical works attempted to relate reconnection onset to the plasma sheet oblique kink mode [*Galeev and Zelenyi*, 1976; *Zhu and Winglee*, 1996; *Pritchett et al.*, 1996; *Lapenta and Brackbill*, 2000; *Wiegelmann and Büchner*, 2000; *Lapenta*, 2003; *Fujimoto*, 2011]. Reconnection due to the oblique kink mode can be expected as close to the Earthward edge of the plasma sheet as reconnection due to ballooning interchange. In contrast to our observations, however, a $\pi/2$ phase shift between δB_X and δB_Z is expected for the oblique kink mode.

[60] Between 7:30 and 7:39 UT, THEMIS probes observed gradual vanishing of the total pressure gradient around the bending point between 11 and 16 R_E. Analysis of the vertical gradients of the magnetic field in the near-Earth plasma sheet prior to dipolarization using THEMIS probes *Saito et al.* [2010] has suggested a sudden decrease in the magnetic field strength in the equatorial plane. This result showed that while the radial gradient of the total pressure remained the same until few minutes before reconnection, the radial gradient of the B_Z component of the magnetic field was decreasing. Similar observations have been reported recently by *Petrukovich et al.* [2007] and *Sergeev et al.* [2011].

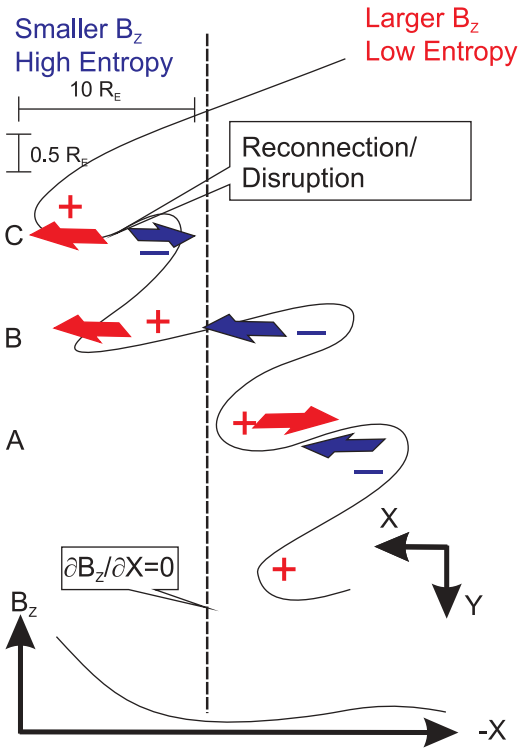

Figure 17. At the top is a sketch illustrating ballooning/interchange fingers obliquely propagating in the Y_{GSM} axis. At the bottom is a schematic profile of the Z_{GSM} component of the magnetic field. Vertical dashed line corresponds to the point where $\partial B_Z/\partial X = 0$. Sketch shows three cases with different finger locations with respect to the point with $\partial B_Z/\partial X = 0$. Depending on the location, the plasma buoyancy force at the adjacent regions of lower and higher entropy will be directed toward each other (case A), parallel (case B), or oppositely (case C). In case C the buoyancy force would pull the fingertip with lower entropy (larger B_Z) further Earthward, while the conjugated space between the fingers with higher entropy (lower B_Z) would be pulled tailward toward the point with $\partial B_Z/\partial X = 0$. Such a configuration could lead to reconnection between the fingertip and the conjugated space between the fingers.

[61] Although the studies by *Erkaev et al.* [2008], *Pritchett and Coroniti* [2010], and *Pritchett and Coroniti* [2011] introduced the negative gradient $\partial B_Z/\partial X$ through a local thinning of the plasma sheet, our observations suggest that it appeared through plasma sheet bending. Therefore, as a final note in Appendix C we develop a simple model of a bent current sheet with finite B_Z that could be used as initial conditions in numerical simulations to further analyze the stability of bent current sheets theoretically.

Appendix A: Solar Wind as a Driver of Plasma Sheet Bending

[62] In this appendix we present evidence that plasma sheet bending was forced by change in the solar wind propagation direction.

[63] The first panel of Figure A1 shows the solar wind propagation direction (black curve) and the orientation of the plasma sheet downtail from $X = -10R_E$ (red curve) according to the AM-03 model in the noon meridian GSM plane on 28 February 2008 between 6:50 and 7:50 UT. The change in plasma sheet orientation after 7:10 UT occurred simultaneously with the change in the solar wind propagation direction. More specifically, the more distant part of the magnetotail moved northward when the initial negative Z_{GSM} component of the solar wind velocity vanished (not shown here).

[64] In the next two panels in Figure A1 one can see that the amplitude of the oscillation in the X_{GSM} component of the magnetic field grew several times with plasma sheet bending. Since some of this growth may be because the

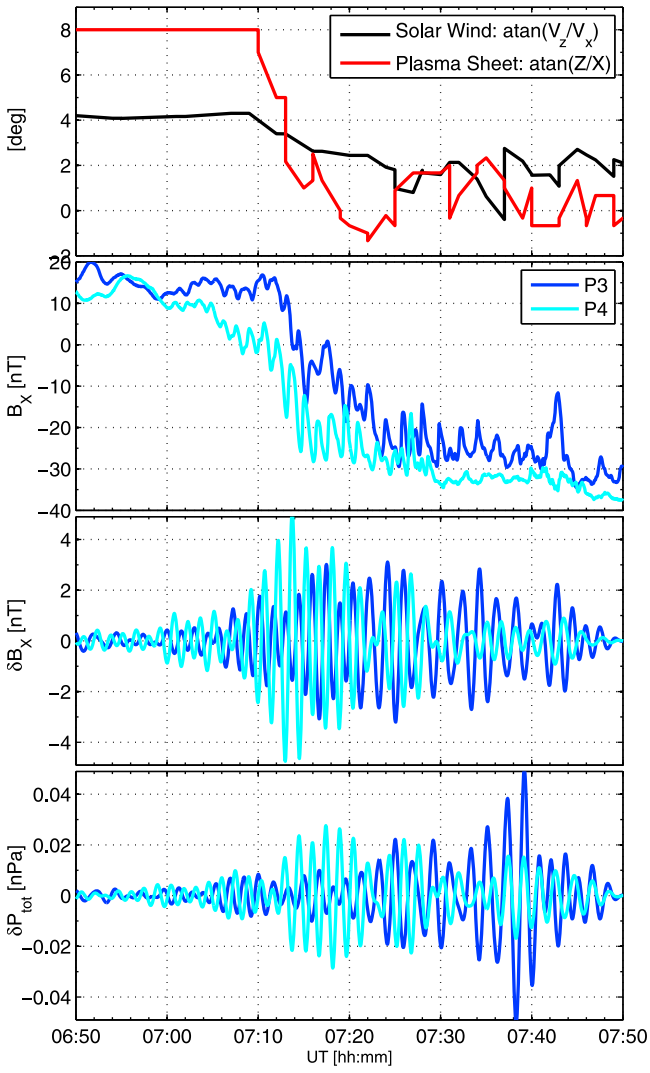

Figure A1. From top to bottom are shown solar wind propagation direction (black) and orientation of the plasma sheet tailward 15 R_E (red) according to the AM-03 model in the noon meridian GSM plane and P3 and P4 observations of the X_{GSM} component of the magnetic field, of the oscillations' amplitude in the X_{GSM} component of the magnetic field, and of the oscillations' amplitude in the total pressure with periods near 100 s on 28 February 2008, between 6:50 and 7:50 UT (see legends for color coding).

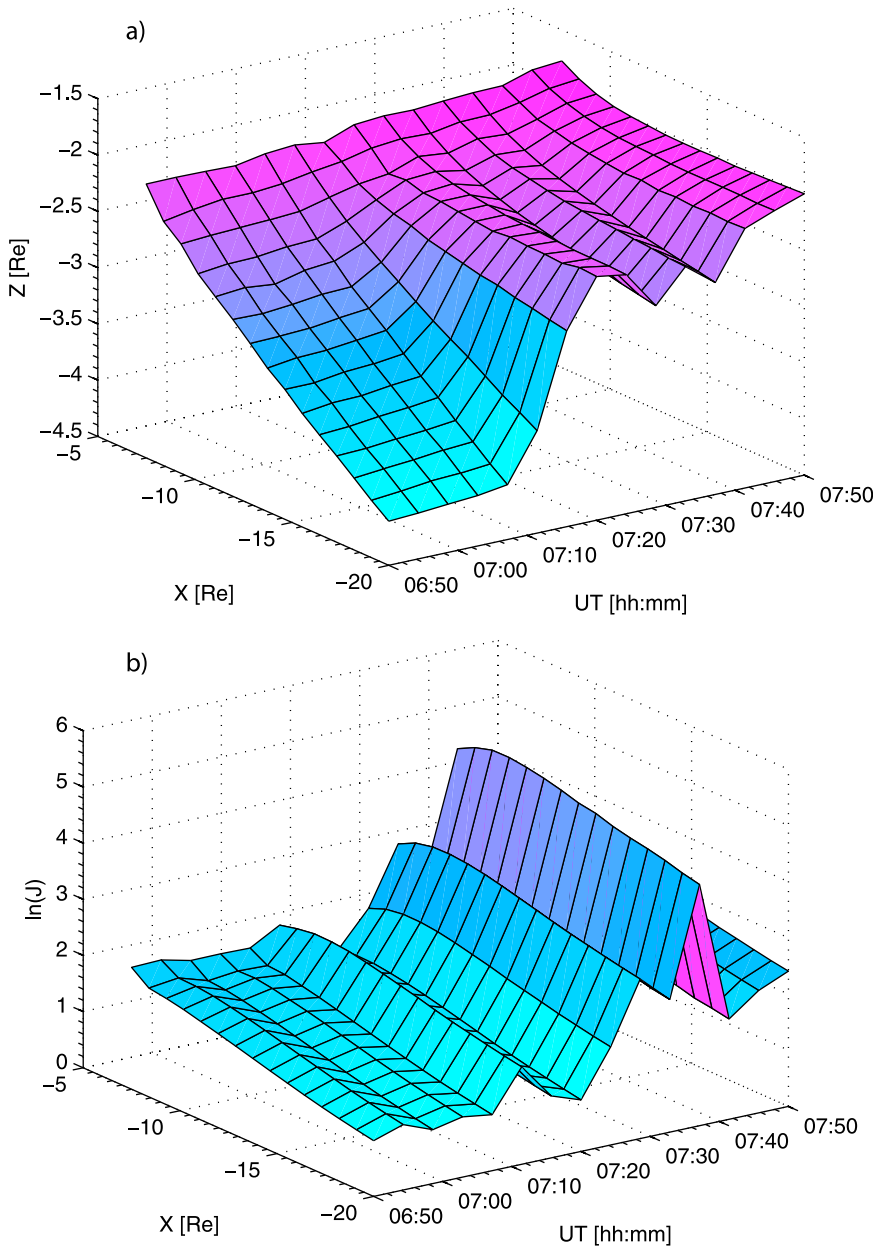

Figure A2. (a) Z_{GSM} coordinate of the neutral sheet for the midnight meridian and (b) natural logarithm of the current density at the neutral sheet depending on the X_{GSM} coordinate and on UT according to the AM-03 model on 28 February 2008between 6:50 and 7:50 UT.

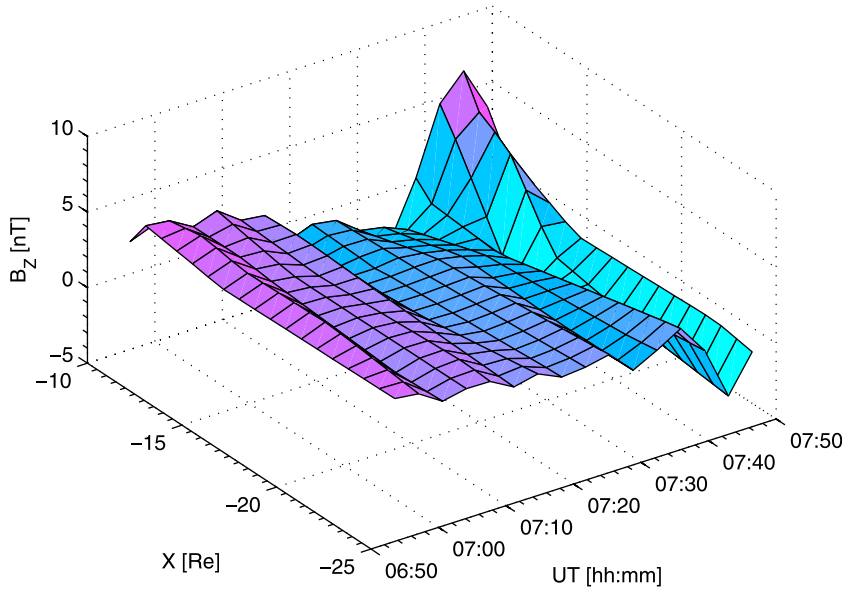

Figure A3. Z_{GSM} component of the magnetic field projected onto the local neutral sheet normal and interpolated between the P1–P4 THEMIS and GOES 11 spacecraft depending on the X_{GSM} coordinate and on UT on 28 February 2008 between 6:50 and 7:50 UT.

probes were located close to the neutral sheet (during the bending), or because they moved far southward of the neutral sheet (after 7:30 UT), we also show that these oscillations grow in the total pressure (shown in the fourth panel of Figure A1).

[65] Figure A2a shows the process of plasma sheet bending in the midnight meridian (X, Z) GSM plane in more detail: the Z_{GSM} coordinate of the neutral sheet is shown depending on the X_{GSM} coordinate and on universal time. The bending between 7:10 and 7:20 UT separates two rather stable neutral sheet locations. Figure A2b shows the current density at the neutral sheet as predicted by the AM-03 model in the same layout. The major growth of the plasma sheet current density occurred after bending, between 7:20 and 7:38 UT. The highest current density values were reached around the point of bending (at $X = -9R_E$), as shown in Figure A2b. After 7:38 UT the plasma sheet current rapidly decreased.

[66] Figure A3 shows the values of $\partial B_Z/\partial X$. To plot this figure, we projected the magnetic field vector measured by five THEMIS probes onto the normal to the plasma sheet neutral plane, as predicted by the AM-03 model (Figure A2a), and interpolated between the radial distances covered by the probes. In Figure A3 at the beginning of the considered time interval; i.e., between 6:50 and 7:10 UT, the $\partial B_Z/\partial X$ on the scales of the interprobe distances was largely positive or neutral. At bending (after 7:20 UT), $\partial B_Z/\partial X$ became significantly negative. Moreover, it continued to decrease until about 7:30 UT, when the plasma sheet current density reached its peak values (cf. Figure A2b).

Appendix B: Spatial Gradient of B_Z as Correlation Coefficient Between Magnetic Field Oscillation and Electron Velocity

[67] In this appendix we show that the directly measured $\partial B_Z/\partial t$ and the X component of the electron velocity are expected to be proportional to each other with the coefficient of proportionality $\partial B_Z/\partial x$.

[68] One can write the Ohm's law in the following form [cf., e.g., *Kadomtsev*, 1976]:

$$\nabla p_e = -en\mathbf{E} - \frac{en}{c}[\mathbf{v}\times\mathbf{B}] + \frac{1}{c}[\mathbf{j}\times\mathbf{B}]. \tag{B1}$$

[69] If we assume that the electron temperature $T_e = const$, then

$$\frac{\nabla p_e}{en} = \nabla\left(\frac{T_e}{e}\ln n\right). \tag{B2}$$

[70] Taking into account that $\mathbf{j} = en(\mathbf{v_i} - \mathbf{v_e})$, one can rewrite equation (B1) in the following form:

$$\mathbf{E} = \frac{1}{c}[\mathbf{v_e}\times\mathbf{B}] - \nabla\left(\frac{T_e}{e}\ln n\right). \tag{B3}$$

[71] Recalling Ampere's law we obtain

$$\frac{\partial \mathbf{B}}{\partial t} = \nabla\times[\mathbf{v_e}\times\mathbf{B}]. \tag{B4}$$

[72] If we define that $\mathbf{v}_e = \mathbf{v}_{e0} + \mathbf{v}_{e1}$ and $\mathbf{B} = \mathbf{B}_0 + \mathbf{B}_1$, where subscript 1 refers to the perturbation components of the electron velocity and the magnetic field, one can write that

$$\frac{\partial B_{1z}}{\partial t} = -\frac{\partial}{\partial x}(v_{e1x}\cdot B_{0z}) + B_{0x}\frac{\partial v_{e1z}}{\partial x} - \frac{\partial}{\partial y}\cdot\left(v_{e1y}\cdot B_{0z} + v_{e0y}\cdot B_{1z}\right). \tag{B5}$$

[73] Here we assume that $\mathbf{v}_{e0} = v_{e0y}\mathbf{e}_y$, $\mathbf{B}_0 = B_{0x}(z)\mathbf{e}_x + B_{0z}(x)\mathbf{e}_z$, and neglecting the second and third terms in equation (B5), one can estimate that

$$\frac{\partial B_{1z}}{\partial t} \approx -v_{e1x}\frac{\partial B_{0z}}{\partial x}. \tag{B6}$$

[74] Hence, knowing $\partial B_{1z}/\partial t$ and v_{e1x} from *in situ* observations one can speculate about the spatial gradient $\partial B_{0z}/\partial x \approx -(1/v_{e1x})\partial B_{1z}/\partial t$. We note that the obtained value

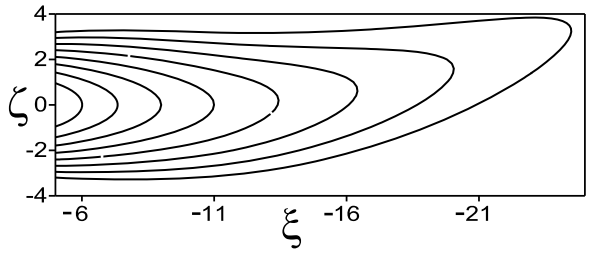

Figure C1. Example of a bent current sheet produced by the model developed in Appendix C.

could be used only as a rough estimate due to numerous assumptions in the derivation of equation (B6).

Appendix C: Analytical Model of a Bent Current Sheet

[75] In this appendix we suggest an analytical model of a bent current sheet, which can be taken as initial conditions in numerical simulations used to investigate the stability of this class of current sheets.

[76] Following *Birn et al.* [1975] we started with the Grad-Shafranov equation

$$\Delta A = -4\pi \frac{dp}{dA}, \tag{C1}$$

where $A = A(x, z)$ is the y component of the vector potential, and $p = p(A)$ is the plasma pressure. We assumed that $\partial A/\partial z \gg \partial A/\partial x$; i.e., the magnetotail is sufficiently stretched. A general solution of this equation was obtained by *Schindler and Birn* [1978]. We use a simplified form of this solution for the magnetotail without gradient $\partial A/\partial y$:

$$A = \sqrt{8\pi p_b L^2}\ln\left\{\frac{\cosh\{f(x)(\zeta - \zeta_0(x))\}}{f(x)}\right\}, \tag{C2}$$

where $f(x) = \sqrt{p_0(x)/p_b}$, $\zeta = z/L$, L is current sheet thickness, $8\pi p_b = B_0^2$, $p_0(x)$ is the plasma pressure at the neutral plane, and $\zeta_0(x)$ is a dimensionless coordinate of the neutral plane.

[77] Then the equations for the magnetic field components can be written as:

$$B_x = \frac{\partial A}{\partial z} = B_0 \tanh\{f(x)(\zeta - \zeta_0(x))\}, \tag{C3}$$

$$B_z = -\frac{\partial A}{\partial x} = B_0\left\{\frac{f'(x)}{f(x)} - \{f'(x)(\zeta - \zeta_0(x)) - f(x)\zeta_0'(x)\} \cdot \tanh\{f(x)(\zeta - \zeta_0(x))\}\right\}. \tag{C4}$$

[78] If we introduce a dimensionless variable $\xi = x/L_x$ and $\nu = L/L_x \ll 1$, one can rewrite the equations for the magnetic field components in the following way:

$$B_x = B_0 \tanh\{f(\xi)(\zeta - \zeta_0(\xi))\}, \tag{C5}$$

$$B_z = B_0\nu\left\{\frac{f'(\xi)}{f(\xi)} - \{f'(\xi)(\zeta - \zeta_0(\xi)) - f(\xi)\zeta_0'(\xi)\} \cdot \tanh\{f(\xi)(\zeta - \zeta_0(\xi))\}\right\}. \tag{C6}$$

[79] Following *Zwingmann* [1983] we chose $f(\xi) = (-\xi)^{-h}$ and obtained that

$$B_x = B_0 \tanh\left\{\frac{(\zeta - \zeta_0(\xi))}{(-\xi)^h}\right\}, \tag{C7}$$

$$B_z = B_0\nu h\left\{\frac{1}{-\xi} - \left\{\frac{\zeta - \zeta_0(\xi)}{(-\xi)^{h+1}} - \frac{\zeta_0'(\xi)}{h(-\xi)^h}\right\}\tanh\left\{\frac{\zeta - \zeta_0(\xi)}{(-\xi)^h}\right\}\right\}. \tag{C8}$$

[80] To create a knee in the current sheet, we took $\zeta_0(x) = \hat{\zeta}_0(\xi - \xi_0)^2$, $\xi < \xi_0$ and $\zeta_0(x) = 0$, $\xi > \xi_0$, where $\hat{\zeta}_0$ and ξ_0 are some constants.

[81] The field lines of the bent current sheet built in this way are presented in Figure C1.

[82] **Acknowledgments.** We acknowledge NASA contract NAS5-02099 for use of data from the THEMIS Mission. Specifically, we thank U. Auster for the use of FGM data provided under the lead of the Technical University of Braunschweig and with financial support through the German Ministry for Economy and Technology and the German Center for Aviation and Space (DLR) under contract 50 OC 0302; C. W. Carlson for use of ESA data; R.P. Lin for use of SST data; J. W. Bonnell and F. S. Mozer for use of EFI data, Howard J. Singer of NOAA Space Weather Prediction Center, and J. H. King and N. Papatashvilli at AdnetSystems, NASA GSFC, and CDAWeb service for GOES 11 and OMNI data. The authors acknowledge P. L. Pritchett for fruitful discussions and J. Hohl for helping with editing. The work was partly supported by the Austrian Science Fund (FWF) I429-N16 and by the Seventh Framework Programme (FP7, project 269198—'Geoplasmas') from the European Commission. The authors acknowledge the reviewer for the insightful comments which have helped to improve the manuscript.

[83] Masaki Fujimoto thanks the reviewers for their assistance in evaluating this paper.

References

Angelopoulos, V. (2008), The THEMIS mission, *Space Sci. Rev.*, *141*, 5–34, doi:10.1007/s11214-008-9336-1.

Angelopoulos, V., W. Baumjohann, C. F. Kennel, F. V. Coronti, M. G. Kivelson, R. Pellat, R. J. Walker, H. Luehr, and G. Paschmann (1992), Bursty bulk flows in the inner central plasma sheet, *J. Geophys. Res.*, *97*, 4027–4039.

Angelopoulos, V., et al. (1994), Statistical characteristics of bursty bulk flow events, *J. Geophys. Res.*, *99*, 21,257–21,280.

Angelopoulos, V., et al. (1996), Multipoint analysis of a bursty bulk flow event on April 11, 1985, *J. Geophys. Res.*, *101*, 4967–4990, doi:10.1029/95JA02722.

Angelopoulos, V., et al. (2008), Tail reconnection triggering substorm onset, *Science*, *321*, 931–935, doi:10.1126/science.1160495.

Artemyev, A. V., A. A. Petrukovich, R. Nakamura, and L. M. Zelenyi (2010), Proton velocity distribution in thin current sheets: Cluster observations and theory of transient trajectories, *J. Geophys. Res.*, *115*, A12255, doi:10.1029/2010JA015702.

Auster, H. U., et al. (2008), The THEMIS fluxgate magnetometer, *Space Sci. Rev.*, *141*, 235–264, doi:10.1007/s11214-008-9365-9.

Baker, D. N., T. I. Pulkkinen, V. Angelopoulos, W. Baumjohann, and R. L. McPherron (1996), Neutral line model of substorms: Past results and present view, *J. Geophys. Res.*, *101*, 12,975–13,010, doi:10.1029/95JA03753.

Baumjohann, W. (2002), Modes of convection in the magnetotail, *Phys. Plasmas*, *9*, 3665–3667, doi:10.1063/1.1499116.

Baumjohann, W., G. Paschmann, and C. A. Cattell (1989), Average plasma properties in the central plasma sheet, *J. Geophys. Res.*, *94*, 6597–6606.

Baumjohann, W., G. Paschmann, and H. Luehr (1990), Characteristics of high-speed ion flows in the plasma sheet, *J. Geophys. Res.*, *95*, 3801–3809.

Baumjohann, W., G. Paschmann, T. Hagai, and H. Luehr (1991), Superposed epoch analysis of the substorm plasma sheet, *J. Geophys. Res.*, *96*, 11,605–11,608, doi:10.1029/91JA00775.

Baumjohann, W., M. Hesse, S. Kokubun, T. Mukai, T. Nagai, and A. A. Petrukovich (1999), Substorm dipolarization and recovery, *J. Geophys. Res.*, *104*, 24,995–25,000, doi:10.1029/1999JA900282.

Baumjohann, W., et al. (2007), Dynamics of thin current sheets: Cluster observations, *Ann. Geophys.*, *25*, 1365–1389, doi:10.5194/angeo-25-1365-2007.

Birn, J., R. Sommer, and K. Schindler (1975), Open and closed magnetospheric tail configurations and their stability, *Astrophys. Space Sci.*, *35*, 389–402, doi:10.1007/BF00637005.

Birn, J., R. Nakamura, E. V. Panov, and M. Hesse (2011), Bursty bulk flows and dipolarization in MHD simulations of magnetotail reconnection, *J. Geophys. Res.*, *116*, A01210, doi:10.1029/2010JA016083.

Bonnell, J. W., F. S. Mozer, G. T. Delory, A. J. Hull, R. E. Ergun, C. M. Cully, V. Angelopoulos, and P. R. Harvey (2008), The Electric Field Instrument (EFI) for THEMIS, *Space Sci. Rev.*, *141*, 303–341.

Chen, C. X., and R. A. Wolf (1999), Theory of thin-filament motion in Earth's magnetotail and its application to bursty bulk flows, *J. Geophys. Res.*, *104*, 14,613–14,626, doi:10.1029/1999JA900005.

Cheng, C. Z., and A. T. Y. Lui (1998), Kinetic ballooning instability for substorm onset and current disruption observed by AMPTE/CCE, *Geophys. Res. Lett.*, *25*, 4091–4094, doi:10.1029/1998GL900093.

Coppi, B., G. Laval, and R. Pellat (1966), Dynamics of the geomagnetic tail, *Phys. Rev. Lett.*, *16*, 1207–1210, doi:10.1103/PhysRevLett.16.1207.

Daughton, W. (1999), Two-fluid theory of the drift kink instability, *J. Geophys. Res.*, *104*, 28,701–28,708, doi:10.1029/1999JA900388.

Du, J., T. L. Zhang, R. Nakamura, C. Wang, W. Baumjohann, A. M. Du, M. Volwerk, K.-H. Glassmeier, and J. P. McFadden (2011), Mode conversion between Alfvén and slow waves observed in the magnetotail by THEMIS, *Geophys. Res. Lett.*, *38*, L07101, doi:10.1029/2011GL046989.

Erkaev, N. V., V. S. Semenov, and H. K. Biernat (2008), Magnetic double gradient mechanism for flapping oscillations of a current sheet, *Geophys. Res. Lett.*, *35*, L02111, doi:10.1029/2007GL032277.

Fujimoto, K. (2011), Dissipation mechanism in 3D magnetic reconnection, *Phys. Plasmas*, *18*, 111206, doi:10.1063/1.3642609.

Galeev, A. A., and L. M. Zelenyi (1976), Nonlinear instability theory for a diffusive neutral layer, *Sov. Phys. JETP*, Engl. Transl., *42*, 450–456.

Galeev, A. A., L. M. Zelenyi, and M. M. Kuznetsova (1985), Nonlinear drift tearing mode: Hard onset and stabilization mechanisms, *JETP Lett.*, *41*, 387–391.

Hayakawa, H., A. Nishida, E. W. Hones Jr., and S. J. Bame (1982), Statistical characteristics of plasma flow in the magnetotail, *J. Geophys. Res.*, *87*, 277–283.

Hu, B., R. A. Wolf, F. R. Toffoletto, J. Yang, and J. Raeder (2011), Consequences of violation of frozen-in-flux: Evidence from OpenGGCM simulations, *J. Geophys. Res.*, *116*, A06223, doi:10.1029/2011JA016667.

Hurricane, O. A., B. H. Fong, S. C. Cowley, F. V. Coroniti, C. F. Kennel, and R. Pellat (1999), Substorm detonation, *J. Geophys. Res.*, *104*, 10,221–10,232, doi:10.1029/1999JA900012.

Kadomtsev, B. B. (1976), *Collective Phenomena in Plasma*, Nauka, Moscow.

Karimabadi, H., W. Daughton, P. L. Pritchett, and D. Krauss-Varban (2003a), Ion-ion kink instability in the magnetotail: 1. Linear theory, *J. Geophys. Res.*, *108*(A11), 1400, doi:10.1029/2003JA010026.

Karimabadi, H., P. L. Pritchett, W. Daughton, and D. Krauss-Varban (2003b), Ion-ion kink instability in the magnetotail: 2. Three-dimensional full particle and hybrid simulations and comparison with observations, *J. Geophys. Res.*, *108*(A11), 1401, doi:10.1029/2003JA010109.

Kaufmann, R. L., and W. R. Paterson (2008), Ion heat flux and energy transport near the magnetotail neutral sheet, *J. Geophys. Res.*, *113*, A05207, doi:10.1029/2007JA012929.

Kaufmann, R. L., W. R. Paterson, and L. A. Frank (2005), Relationships between the ion flow speed, magnetic flux transport rate, and other plasma sheet parameters, *J. Geophys. Res.*, *110*, A09216, doi:10.1029/2005JA011068.

Keika, K., et al. (2009), Observations of plasma vortices in the vicinity of flow-braking: A case study, *Ann. Geophys.*, *27*, 3009–3017.

Keiling, A., et al. (2009), Substorm current wedge driven by plasma flow vortices: THEMIS observations, *J. Geophys. Res.*, *114*, A00C22, doi:10.1029/2009JA014114.

Korovinskiy, D. B., V. V. Ivanova, N. V. Erkaev, V. S. Semenov, I. B. Ivanov, H. K. Biernat, and M. Zellinger (2011), Kink-like mode of a double gradient instability in a compressible plasma current sheet, *Adv. Space Res.*, *48*, 1531–1536, doi:10.1016/j.asr.2011.07.008.

Kubyshkina, M., V. Sergeev, N. Tsyganenko, V. Angelopoulos, A. Runov, H. Singer, K. H. Glassmeier, H. U. Auster, and W. Baumjohann (2009), Toward adapted time-dependent magnetospheric models: A simple approach based on tuning the standard model, *J. Geophys. Res.*, *114*, A00C21, doi:10.1029/2008JA013547.

Kubyshkina, M., V. Sergeev, N. Tsyganenko, V. Angelopoulos, A. Runov, E. Donovan, H. Singer, U. Auster, and W. Baumjohann (2011), Time-dependent magnetospheric configuration and breakup mapping during a substorm, *J. Geophys. Res.*, *116*, A00I27, doi:10.1029/2010JA015882.

Lapenta, G. (2003), A new paradigm for 3D collisionless magnetic reconnection, *Space Sci. Rev.*, *107*, 167–174, doi:10.1023/A:1025579923977.

Lapenta, G., and J. U. Brackbill (1997), A kinetic theory for the drift-kink instability, *J. Geophys. Res.*, *102*, 27,099–27,108, doi:10.1029/97JA02140.

Lapenta, G., and J. U. Brackbill (2000), 3D reconnection due to oblique modes: A simulation of Harris current sheets, *Nonlinear Processes Geophys.*, *7*, 151–158.

Liang, J., E. F. Donovan, W. W. Liu, B. Jackel, M. Syrjäsuo, S. B. Mende, H. U. Frey, V. Angelopoulos, and M. Connors (2008), Intensification of preexisting auroral arc at substorm expansion phase onset: Wave-like disruption during the first tens of seconds, *Geophys. Res. Lett.*, *35*, L17S19, doi:10.1029/2008GL033666.

Lui, A. T. Y. (1996), Current disruption in the Earth's magnetosphere: Observations and models, *J. Geophys. Res.*, *101*, 13,067–13,088, doi:10.1029/96JA00079.

Lui, A. T. Y., et al. (1992), Current disruptions in the near-Earth neutral sheet region, *J. Geophys. Res.*, *97*, 1461–1480, doi:10.1029/91JA02401.

McFadden, J. P., C. W. Carlson, D. Larson, V. Angelopoulos, M. Ludlam, R. Abiad, B. Elliot, P. Turin, and M. Marckwordt (2008), The THEMIS ESA plasma instrument and in-flight calibration, *Space Sci. Rev.*, *141*, 277–302.

Mishin, V. M., T. Saifudinova, A. Bazarzhapov, C. T. Russell, W. Baumjohann, R. Nakamura, and M. Kubyshkina (2001), Two distinct substorm onsets, *J. Geophys. Res.*, *106*, 13,105–13,118, doi:10.1029/2000JA900152.

Nagai, T., M. Fujimoto, R. Nakamura, W. Baumjohann, A. Ieda, I. Shinohara, S. Machida, Y. Saito, and T. Mukai (2005), Solar wind control of the radial distance of the magnetic reconnection site in the magnetotail, *J. Geophys. Res.*, *110*, A09208, doi:10.1029/2005JA011207.

Nakamura, R., D. N. Baker, D. H. Fairfield, D. G. Mitchell, R. L. McPherron, and E. W. Hones Jr. (1994), Plasma flow and magnetic field characteristics near the midtail neutral sheet, *J. Geophys. Res.*, *99*, 23,591–23,601.

Nakamura, R., et al. (2002), Fast flow during current sheet thinning, *Geophys. Res. Lett.*, *29*(23), 2140, doi:10.1029/2002GL016200.

Nakamura, R., et al. (2004), Spatial scale of high-speed flows in the plasma sheet observed by Cluster, *Geophys. Res. Lett.*, *31*, L09804, doi:10.1029/2004GL019558.

Nakamura, R., et al. (2011), Flux transport, dipolarization, and current sheet evolution during a double-onset substorm, *J. Geophys. Res.*, *116*, A00I36, doi:10.1029/2010JA015865.

Ohtani, S., H. J. Singer, and T. Mukai (2006), Effects of the fast plasma sheet flow on the geosynchronous magnetic configuration: Geotail and GOES coordinated study, *J. Geophys. Res.*, *111*, A01204, doi:10.1029/2005JA011383.

Panov, E. V., et al. (2010a), Plasma sheet thickness during a bursty bulk flow reversal, *J. Geophys. Res.*, *115*, A05213, doi:10.1029/2009JA014743.

Panov, E. V., et al. (2010b), Multiple overshoot and rebound of a bursty bulk flow, *Geophys. Res. Lett.*, *37*, L08103, doi:10.1029/2009GL041971.

Petrukovich, A. A., W. Baumjohann, R. Nakamura, T. Mukai, and O. A. Troshichev (2000), Small substorms: Solar wind input and magnetotail dynamics, *J. Geophys. Res.*, *105*, 21,109–21,118, doi:10.1029/2000JA900057.

Petrukovich, A. A., T. L. Zhang, W. Baumjohann, R. Nakamura, A. Runov, A. Balogh, and C. Carr (2006), Oscillatory magnetic flux tube slippage in the plasma sheet, *Ann. Geophys.*, *24*, 1695–1704, doi:10.5194/angeo-24-1695-2006.

Petrukovich, A. A., W. Baumjohann, R. Nakamura, A. Runov, A. Balogh, and H. Rème (2007), Thinning and stretching of the plasma sheet, *J. Geophys. Res.*, *112*, A10213, doi:10.1029/2007JA012349.

Petrukovich, A. A., W. Baumjohann, R. Nakamura, and A. Runov (2008), Formation of current density profile in tilted current sheets, *Ann. Geophys.*, *26*, 3669–3676, doi:10.5194/angeo-26-3669-2008.

Petrukovich, A. A., W. Baumjohann, R. Nakamura, and H. Rème (2009), Tailward and Earthward flow onsets observed by Cluster in a thin current sheet, *J. Geophys. Res.*, *114*, A09203, doi:10.1029/2009JA014064.

Petrukovich, A. A., A. V. Artemyev, H. V. Malova, V. Y. Popov, R. Nakamura, and L. M. Zelenyi (2011), Embedded current sheets in the Earth's magnetotail, *J. Geophys. Res.*, *116*, A00I25, doi:10.1029/2010JA015749.

Pritchett, P. L., and F. V. Coroniti (2010), A kinetic ballooning/interchange instability in the magnetotail, *J. Geophys. Res.*, *115*, A06301, doi:10.1029/2009JA014752.

Pritchett, P. L., and F. V. Coroniti (2011), Plasma sheet disruption by interchange-generated flow intrusions, *Geophys. Res. Lett.*, *38*, L10102, doi:10.1029/2011GL047527.

Pritchett, P. L., F. V. Coroniti, and V. K. Decyk (1996), Three-dimensional stability of thin quasi-neutral current sheets, *J. Geophys. Res.*, *101*, 27,413–27,430, doi:10.1029/96JA02665.

Roux, A., et al. (1991), Plasma sheet instability related to the westward traveling surge, *J. Geophys. Res.*, *96*, 17,697–17,714, doi:10.1029/91JA01106.

Runov, A., et al. (2005), Electric current and magnetic field geometry in flapping magnetotail current sheets, *Ann. Geophys.*, *23*, 1391–1403, doi:10.5194/angeo-23-1391-2005.

Runov, A., V. Angelopoulos, V. A. Sergeev, K. Glassmeier, U. Auster, J. McFadden, D. Larson, and I. Mann (2009), Global properties of magnetotail current sheet flapping: THEMIS perspectives, *Ann. Geophys.*, *27*, 319–328, doi:10.5194/angeo-27-319-2009.

Saito, M. H., Y. Miyashita, M. Fujimoto, I. Shinohara, Y. Saito, and T. Mukai (2008), Modes and characteristics of low-frequency MHD waves in the near-Earth magnetotail prior to dipolarization: Fitting method, *J. Geophys. Res.*, *113*, A06201, doi:10.1029/2007JA012778.

Saito, M. H., L.-N. Hau, C.-C. Hung, Y.-T. Lai, and Y.-C. Chou (2010), Spatial profile of magnetic field in the near-Earth plasma sheet prior to dipolarization by THEMIS: Feature of minimum B, *Geophys. Res. Lett.*, *37*, L08106, doi:10.1029/2010GL042813.

Schindler, K. (1974), A theory of the substorm mechanism, *J. Geophys. Res.*, *79*, 2803–2810, doi:10.1029/JA079i019p02803.

Schindler, K., and J. Birn (1978), Magnetospheric physics, *Phys. Rep.*, *47*, 109–165, doi:10.1016/0370-1573(78)90016-9.

Schödel, R., W. Baumjohann, R. Nakamura, V. A. Sergeev, and T. Mukai (2001a), Rapid flux transport in the central plasma sheet, *J. Geophys. Res.*, *106*, 301–314, doi:10.1029/2000JA900139.

Schödel, R., R. Nakamura, W. Baumjohann, and T. Mukai (2001b), Rapid flux transport and plasma sheet reconfiguration, *J. Geophys. Res.*, *106*, 8381–8390, doi:10.1029/2000JA900159.

Sergeev, V. A., V. Angelopoulos, J. T. Gosling, C. A. Cattell, and C. T. Russell (1996), Detection of localized, plasma-depleted flux tubes or bubbles in the midtail plasma sheet, *J. Geophys. Res.*, *101*, 10,817–10,826, doi:10.1029/96JA00460.

Sergeev, V. A., D. A. Sormakov, S. V. Apatenkov, W. Baumjohann, R. Nakamura, A. V. Runov, T. Mukai, and T. Nagai (2006), Survey of large-amplitude flapping motions in the midtail current sheet, *Ann. Geophys.*, *24*, 2015–2024, doi:10.5194/angeo-24-2015-2006.

Sergeev, V., et al. (2008), Study of near-Earth reconnection events with Cluster and Double Star, *J. Geophys. Res.*, *113*, A07S36, doi:10.1029/2007JA012902.

Sergeev, V., V. Angelopoulos, M. Kubyshkina, E. Donovan, X.-Z. Zhou, A. Runov, H. Singer, J. McFadden, and R. Nakamura (2011), Substorm growth and expansion onset as observed with ideal ground-spacecraft THEMIS coverage, *J. Geophys. Res.*, *116*, A00I26, doi:10.1029/2010JA015689.

Sitnov, M. I., and K. Schindler (2010), Tearing stability of a multiscale magnetotail current sheet, *Geophys. Res. Lett.*, *37*, L08102, doi:10.1029/2010GL042961.

Snekvik, K., et al. (2007), Cluster observations of a field aligned current at the dawn flank of a bursty bulk flow, *Ann. Geophys.*, *25*, 1405–1415.

Takada, T., et al. (2006), Do BBFs contribute to inner magnetosphere dipolarizations: Concurrent Cluster and Double Star observations, *Geophys. Res. Lett.*, *33*, L21109, doi:10.1029/2006GL027440.

Wiegelmann, T., and J. Büchner (2000), Kinetic simulations of the coupling between current instabilities and reconnection in thin current sheets, *Nonlinear Processes Geophys.*, *7*, 141–150.

Yang, J., R. A. Wolf, and F. R. Toffoletto (2011), Accelerated thinning of the near-Earth plasma sheet caused by a bubble-blob pair, *Geophys. Res. Lett.*, *38*, L01107, doi:10.1029/2010GL045993.

Zelenyi, L., A. Artemiev, H. Malova, and V. Popov (2008), Marginal stability of thin current sheets in the Earth's magnetotail, *J. Atmos. Sol. Terr. Phys.*, *70*, 325–333, doi:10.1016/j.jastp.2007.08.019.

Zelenyi, L. M., A. V. Artemyev, A. A. Petrukovich, R. Nakamura, H. V. Malova, and V. Y. Popov (2009), Low frequency eigenmodes of thin anisotropic current sheets and Cluster observations, *Ann. Geophys.*, *27*, 861–868, doi:10.5194/angeo-27-861-2009.

Zelenyi, L. M., A. V. Artemyev, K. V. Malova, A. A. Petrukovich, and R. Nakamura (2010), Metastability of current sheets, *Phys. Usp.*, *53*, 933–941, doi:10.3367/UFNe.0180.201009g.0973.

Zhang, T. L., W. Baumjohann, R. Nakamura, A. Balogh, and K.-H. Glassmeier (2002), A wavy twisted neutral sheet observed by CLUSTER, *Geophys. Res. Lett.*, *29*(19), 1899, doi:10.1029/2002GL015544.

Zhu, Z., and R. M. Winglee (1996), Tearing instability, flux ropes, and the kinetic current sheet kink instability in the Earth's magnetotail: A three-dimensional perspective from particle simulations, *J. Geophys. Res.*, *101*, 4885–4898, doi:10.1029/95JA03144.

Zwingmann, W. (1983), Self-consistent magnetotail theory: Equilibrium structures including arbitrary variation along the tail axis, *J. Geophys. Res.*, *88*, 9101–9108, doi:10.1029/JA088iA11p09101.